Research Paper

Causes of Cretaceous subduction termination below South China and Borneo: Was the Proto-South China Sea underlain by an oceanic plateau?

Suzanna H.A. van de Lagemaat [a,*], Licheng Cao [b], Junaidi Asis [c], Eldert L. Advokaat [a], Paul R.D. Mason [a], Mark J. Dekkers [a], Douwe J.J. van Hinsbergen [a]

[a] Department of Earth Sciences, Utrecht University, Utrecht, the Netherlands
[b] College of Marine Science and Technology, China University of Geosciences, Wuhan, China
[c] Faculty of Science and Natural Resources, Universiti Malaysia Sabah, Kota Kinabalu, Malaysia

ABSTRACT

The South China, Indochina, and Borneo margins surrounding the South China Sea contain long-lived arcs that became inactive at approximately 85 Ma, even though an embayment of oceanic crust (the 'Proto-South China Sea') remained in the intervening region. This oceanic crust eventually subducted in the Cenozoic below Borneo and the Cagayan arc, while the modern South China Sea opened in its wake. To investigate the enigmatic cessation of Mesozoic subduction below South China and Borneo, we studied a fragment of oceanic crust and overlying trench-fill sediments that accreted to NW Borneo during the final stages of Paleo-Pacific subduction. Based on radiolarian biostratigraphy of cherts overlying the pillow basalts and detrital zircon geochronology of the trench-fill, we constrained the minimum age of the oceanic crust during accretion to 40 Ma. This shows that subduction cessation was not related to ridge subduction. Geochemical analysis of pillow basalts revealed an enriched mid-ocean ridge basalt signature comparable to oceanic plateaus. Using paleomagnetism, we show that this fragment of oceanic crust was not part of the Izanagi Plate but was part of a plate (the 'Pontus' Plate) separated from the Izanagi Plate by a subduction zone. Based on the minimum 40 Ma age of the oceanic crust and its geochemistry, we suggest that Mesozoic subduction below South China and Borneo stopped when an oceanic plateau entered the trench, while the eastern plate margin with the Izanagi Plate remained active. We show how our findings offer opportunities to restore plate configurations of the Panthalassa-Tethys junction region.

© 2023 China University of Geosciences (Beijing) and Peking University. Published by Elsevier B.V. on behalf of China University of Geosciences (Beijing). This is an open access article under the CC BY-NC-ND license (http://creativecommons.org/licenses/by-nc-nd/4.0/).

1. Introduction

For the last hundreds of millions of years, the East Asian margin has been accommodating subduction of Paleo-Pacific (or 'Panthalassa') lithosphere (Isozaki et al., 1990; Isozaki et al., 2010). Today, the subduction zone along the east Asian margin continues as far as Taiwan region (China), where it connects to plate boundaries of the Philippines. However, geological records of arc magmatism and accretionary complexes show that until the Late Cretaceous (∼80 Ma) a Paleo-Pacific subduction zone was active along South China, through Hainan, Vietnam and Cambodia as far as southern Borneo (e.g., Jahn et al., 1990; Lapierre et al., 1997; Xu et al., 1999; Shellnutt et al., 2013, 2023; Li et al., 2014b; Li et al., 2014c; Breitfeld et al., 2017; Hennig et al., 2017; Cao et al., 2021a; Hennig-Breitfeld et al., 2021; Nong et al., 2021, 2022;

Waight et al., 2021; Hieu et al., 2022; Zhou et al., 2023). Then, around 80–70 Ma, Paleo-Pacific subduction at the SE China and Indochina margin appears to have ceased, the South China and Vietnamese margins became passive, Paleogene rift basins formed, and after the Eocene, the South China Sea extensional basin opened (Barckhausen et al., 2014; Li et al., 2014a; Morley, 2016; Wu et al., 2016; Ye et al., 2018). Why Cretaceous subduction stopped, and where the ensuing convergence between the plates from the Pacific realm and Eurasia was accommodated, is poorly known.

Clues as to why subduction ceased come from rock units of the subducted Paleo-Pacific plates (Ocean Plate Stratigraphy (OPS); Isozaki et al., 1990) preserved in accretionary prisms. Relics of Late Cretaceous and older prisms are found on Taiwan region, China (Yui et al., 2012), along the South China margin west of Taiwan region, China (Zhou et al., 2006a), and to the south of the South China Sea in Palawan (e.g., Holloway, 1982; Shao et al., 2017; Fig. 1). The South China margin reveals that during the final stages of subduction, lithosphere with seamounts as old as 154.1 ± 1.8 Ma

* Corresponding author.
    E-mail address: s.h.a.vandelagemaat@uu.nl (S.H.A. van de Lagemaat).

accreted (Xu et al., 2022). In addition, the Palawan record concerns a fragment of the South China margin that became separated from its original position by opening of the South China Sea basin within the SE China continental margin during the latest Eocene to middle Miocene (Briais et al., 1993; Suggate et al., 2014; Li et al., 2015; Shao et al., 2017; Larsen et al., 2018). The Eocene to Miocene opening of the South China Sea basin was accommodated by a southward-dipping subduction zone below northern Borneo and the Cagayan arc (Hall, 2002; Hall and Breitfeld, 2017) (Fig. 1C). Rock units that accreted during this southward subduction include ∼100 Ma old mafic rocks and Lower Cretaceous pelagic sediments (Muller, 1991; Dycoco et al., 2021) that are overlain by a continuous Upper Cretaceous (Campanian–Maastrichtian) pelagic oceanic sequence and Eocene trench-fill sediments (Wolfart et al., 1986; Aurelio et al., 2014). This shows that after Cretaceous subduction cessation at the South China-Borneo margin, there oceanic lithosphere remained in the foreland embayment of the former subduction zone that already existed before Cretaceous subduction cessation, and that remained in an oceanic position until it was finally consumed by renewed subduction in the Eo-Oligocene. This oceanic embayment that remained after Cretaceous subduction cessation and that was consumed during Eocene to Miocene subduction below Borneo and the Cagayan arc is referred to as the 'Proto-South China Sea' (Taylor and Hayes, 1983; Hinz et al., 1994; Hall and Breitfeld, 2017). Why the Proto-South China Sea remained in existence during the Late Cretaceous and early Cenozoic while old oceanic lithosphere was still available to subduct (which eventually subducted in the Eocene to Miocene) is puzzling.

Obtaining new geological data to decipher the enigmatic tectonic history of the Paleo-Pacific/Proto-South China Sea from the deformed, poorly exposed, and largely submerged records of the South China margin, Taiwan region (China), and Palawan accre-

tionary prisms is difficult due to their poor preservation, accessibility, and tropical rainforest cover. However, the Proto-South China Sea was also bordered by a former subduction zone associated with Paleo-Pacific subduction to the south. Accretionary records related to this Paleo-Pacific subduction zone are preserved in Sarawak (Serabang Complex, Lubok Antu Complex) and Sabah. There, an accretionary complex expose OPS sequences consisting of pillow basalts, radiolarian cherts, and trench-fill clastics (Jasin, 2000, 2018). These OPS sequences form the youngest part of a Mesozoic accretionary prism adjacent to a Jurassic to Cretaceous volcanic arc exposed in Kuching Zone (Breitfeld et al., 2017), and in the Schwaner Mountains (Hennig et al., 2017; Breitfeld et al., 2020) of the SW Borneo Mega-Unit (Advokaat and Van Hinsbergen, 2023). This prism and arc formed during northward motion of Borneo, as part of a plate carrying continental fragments known as Argoland from the Gondwana margin towards Eurasia (Hall, 2012; Advokaat and Van Hinsbergen, 2023). Intriguingly, Borneo's northward motion towards Eurasia stopped in the Late Cretaceous (Hall, 2012; Advokaat and Van Hinsbergen, 2023), around the time of subduction cessation at the South China margin, 'trapping' oceanic crust in the Proto-South China Sea embayment.

In this study, we investigate the age of the crust of the youngest OPS nappes exposed in the Baliojong Complex in Sabah, North Borneo, using radiolarian biostratigraphy of the chert to determine the minimum age of the oceanic crust, and detrital zircon geochronology of the trench-fill deposits to constrain the age of its accretion. This allows us to determine the minimum age of oceanic crust when it entered the subduction zone. We use major and trace element geochemistry of pillow basalts to investigate the tectonic setting of formation of the ocean floor. Finally, we use paleomagnetism of the pillow basalts and radiolarian chert to constrain the paleolatitude of formation of the oceanic crust. This allows us to test possible connections of the 'Proto-South China Sea' crust
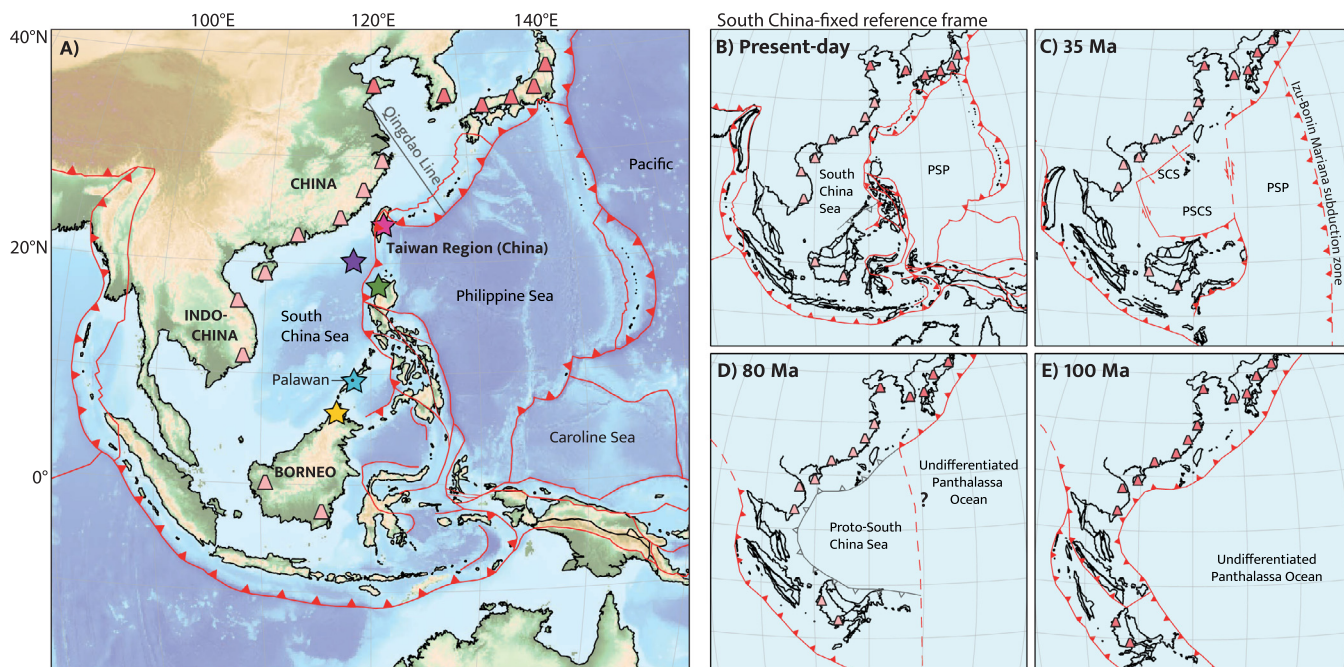

Fig. 1. (A) Present-day map of the (proto-)South China region. Stars mark locations of geological data from the Proto-South China Sea: Yellow – Baliojong River (this study); Blue – South Palawan Ophiolite; Green – Dos Hermanos Mélange; Purple – Accreted seamounts; Pink – Tailuko Belt. Dark pink cones indicate active arc magmatism, light pink cones indicate extinct arc magmatism. Arc magmatism has been continuously active northeast of the Qingdao Line, whereas it went extinct in the Late Mesozoic to the southwest of this line. (B–E) Simplified Late Mesozoic – Cenozoic tectonic evolution of the proto-South China region, based on the reconstruction of Advokaat and Van Hinsbergen (2023), in a South China-fixed reference frame. Active plate boundaries are shown in red, former plate boundaries in gray. Dark pink cones indicate active arc magmatism, light pink cones indicate extinct arc magmatism. Background image is ETOPO 2022 15 Arc-Second Global Relief Model. (NOAA National Centers for Environmental Information, 2022). PSP: Philippine Sea Plate; PSCS: Proto-South China Sea. (For interpretation of the references to colour in this figure legend, the reader is referred to the web version of this article.)

to the Tethyan or Paleo-Pacific paleo-plates. In combination with available constraints from Palawan, the South China margin, and Taiwan region (China), we will evaluate possible reasons for the enigmatic cessation of long-lived subduction at the South China-Sundaland margin, and the origin and destruction of the Proto-South China Sea.

2. Geological setting

2.1. Records of arc magmatism related to Paleo-Pacific subduction

A Mesozoic Paleo-Pacific subduction zone below SE China, Indochina and Borneo has been interpreted based on evidence arc magmatism and accretionary complexes. Granitoid emplacement in SE China occurred throughout the Mesozoic (e.g., Zhou et al., 2006b; Ji et al., 2017). For the suite of granites and related volcanics emplaced during the Late Jurassic and Cretaceous it is generally accepted that they formed as a magmatic arc that formed during subduction of Paleo-Pacific oceanic lithosphere (Jahn et al., 1976; Lapierre et al., 1997; Zhou and Li, 2000; Zhou et al., 2006; Li and Li, 2007; Li et al., 2012a; Li et al., 2014b; Jiang et al., 2015; Zhu et al., 2017; Liu et al., 2020a; Sun et al., 2021). Most magmatism in SE China had ceased by ca. 90 Ma, after which limited A-type magmatism occurred until 80 Ma, which was interpreted to reflect extension (Li et al., 2012b, 2014b, 2014c; Liu et al., 2020b). The youngest granite intrusion, with a 73 Ma zircon U-Pb age is exposed on Hainan Island (Jiang and Li, 2014).

The youngest arc magmatism interpreted to be related to Paleo-Pacific subduction below Indochina is most prominent in the Dalat Zone of Vietnam (e.g., Nguyen et al., 2004; Thuy et al., 2004; Shellnutt et al., 2013; Hennig-Breitfeld et al., 2021; Nong et al., 2022). Radiometric dating of these plutons using zircon and titanite U-Pb geochronology revealed ages from 122 Ma to 75 Ma (Nguyen et al., 2004; Shellnutt et al., 2013; Hennig-Breitfeld et al., 2021; Nong et al., 2021). Based on the geochemistry of the igneous rocks in Vietnam and Cambodia, the older magmatic stage (110–89 Ma) that produced calc-alkaline I-type granitic batholiths, is thought to have formed during active subduction, while the younger magmatic stage (87–75 Ma) that produced A-type granites may instead relate to extensional deformation after subduction cessation (Shellnutt et al., 2013; Hennig-Breitfeld et al., 2021; Waight et al., 2021; Nong et al., 2022).

Westernmost Borneo (west Sarawak and NW Kalimantan) has been part of Sundaland since at least the Triassic (e.g., Breitfeld et al., 2017) and was possibly derived from South China (e.g., Metcalfe, 1985). Triassic and Jurassic magmatism and metamorphism in this part of Borneo was interpreted to be related to westward subduction of a Paleo-Pacific plate (Breitfeld et al., 2017; Hennig et al., 2017) predating accretion of the Proto-South China Sea. This sequence is unconformably overlain by Upper Jurassic shallow marine Bau limestone (Kakizaki et al., 2013), and by Upper Jurassic mudstone and radiolarian chert, and Cretaceous deep marine volcaniclastics of the Pedawan Formation (Schmidtke et al., 1990; Jasin and Said, 1999; Breitfeld et al., 2017; Zhang et al., 2022). This sequence was interpreted to record the transition from a passive margin in the Jurassic to a forearc basin in the Late Jurassic to Late Cretaceous (Breitfeld et al., 2017). The sequence is unconformably overlain by Upper Cretaceous (Maastrichtian) or Paleocene to Eocene continental clastics that post-date arc magmatism (Breitfeld et al., 2018; Berry, 2022).

SW Borneo, which was derived from Gondwana, preserves evidence of Jurassic magmatism that was interpreted as being related to rifting of the SW Borneo block (as part of 'Argoland') from Gondwana (Davies et al., 2014; Breitfeld et al., 2020; Batara and Xu, 2022). Subsequent magmatism related to Paleo-Pacific subduction

below Gondwana-derived Borneo is well-exposed in the Schwaner Mountains of SW Borneo (e.g., Breitfeld et al., 2017, 2020; Hennig et al., 2017), and was underway by ca. 132 Ma (Breitfeld et al., 2017, 2020), and perhaps already by 154–150 Ma (Batara and Xu, 2022). In North Borneo, arc magmatism was already active during the Triassic and Jurassic (Burton-Johnson et al., 2020), when the SW Borneo block was still part of the Gondwana margin (Hall, 2012; Advokaat and Van Hinsbergen, 2023). The youngest magmatism that may be related to Paleo-Pacific subduction exposed in the Schwaner Mountains has ages of ca. 77 Ma (Breitfeld et al., 2017, 2020; Qian et al., 2022), but as in South China and Vietnam, A-type granite geochemical signatures in the post-80 Ma plutons in SW Borneo have also been interpreted as extensional magmatism that followed subduction cessation (Breitfeld et al., 2017, 2020).

2.2. OPS records

2.2.1. OPS records of Paleo-Pacific subduction

Information about the oceanic Paleo-Pacific lithosphere that was subducting below SE China and Borneo comes from the accretionary prisms exposed in Taiwan region (China), the northern South China Sea margin, Palawan, and Borneo. There is no accretionary prism related to Paleo-Pacific subduction exposed onshore in China or Vietnam.

Based on gravimetric, magnetic, and wide-angle seismic data, an accretionary complex was interpreted in the NE margin of the South China Sea (Zhou et al., 2006). In this area, relics of two seamounts have been found, which were originally interpreted as Miocene features (e.g., Wang et al., 2012; Xu et al., 2020), but recently yielded plagioclase ^{40}Ar/^{39}Ar plateau ages of 154.1 ± 1.8 Ma and 93.2 ± 5.0 Ma (Xu et al., 2022). These seamounts have ocean island basalt (OIB) geochemistry and are interpreted as intraplate basalts that formed on Paleo-Pacific lithosphere (Xu et al., 2020; Xu et al., 2022). The oldest seamount thus provides a minimum age for the oceanic crust (∼154 Ma) of the Paleo-Pacific lithosphere that was subducting below SE China. The youngest seamount provides a maximum age of accretion (∼93 Ma), i.e., not long before the end of subduction. Xu et al. (2022) suggested that these seamounts may have formed as part of an oceanic plateau.

The submerged accretionary complex in the northern South China Sea may be contiguous with the Tailuko Belt of Taiwan region (China), which is interpreted as a Late Jurassic to Early Cretaceous accretionary complex that formed during Paleo-Pacific subduction below the South China margin (Yui et al., 2012). Here, upper Jurassic to lowermost Cretaceous terrigenous trench-fill clastic sediments overlie Permian greenschist facies interlayers of marble, chert, and metabasite (Yui et al., 2012), interpreted as an OPS sequence. The massive marbles are interpreted as platform deposits, possibly deposited on seamounts or an oceanic plateau (Jahn et al., 1992; Yui et al., 2012). The accretionary prism is intruded by Late Cretaceous granitic plutons, for which ages of 90–87 Ma were obtained (Yui et al., 2009; Yui et al., 2012). The Tailuko Belt is unconformably overlain by Eocene *syn*-rift sediments, which are interpreted as the passive margin sediments of the northern South China Sea margin (Ho, 1986; Conand et al., 2020).

To the south of the South China Sea, the Palawan Continental Terrane is exposed on the Palawan and Calamian Islands, in the Philippines. This 'continental' terrane is a composite terrane that is also interpreted to have formed as an accretionary prism along the SE China Margin (e.g., Holloway, 1982; Shao et al., 2017). After subduction ceased, the Palawan Continental Terrane formed part of the SE China passive margin and was subsequently transported southwards during opening of the South China Sea and became accreted in the Cenozoic accretionary fold-thrust belt that formed

north of the Cagayan arc during southward subduction of the Proto-South China Sea (e.g., Cao et al., 2021a). The Palawan Continental Terrane exposed on the Calamian Islands comprises Permian to Upper Jurassic radiolarian chert, middle Permian to Upper Jurassic limestone, and Middle Jurassic to Lower Cretaceous trench-fill clastic sediments (Zamoras and Matsuoka, 2001, 2004). Based on the lithologic transition from chert to limestone to terrigenous clastic sediments, it was interpreted that these accreted units define a north-to-south younging accretionary prism, which formed during three distinct accretion events in the Middle Jurassic, Late Jurassic, and Early Cretaceous (Zamoras and Matsuoka, 2001, 2004). A Middle Jurassic to Late Jurassic accretionary prism is also exposed on the island of Palawan (Faure and Ishida, 1990) and on the Buruanga Peninsula of Panay (Zamoras et al., 2008). Detrital zircons in the trench-fill turbidites of the Palawan Continental Terrane suggest a South China magmatic arc provenance (Cao et al., 2021b). The Palawan Continental Terrane is overlain by Upper Cretaceous continental clastic sediments with arc-derived detrital zircons interpreted to have been deposited over the prism after subduction ceased. The Upper Cretaceous continental clastics are overlain by Eocene *syn*-rift turbidites with a South China provenance, which are interpreted to reflect the early opening stages of the South China Sea basin. These are overlain by upper Oligocene-lower Miocene limestones that formed during the drift of the Palawan Continental Terrane towards the Palawan subduction zone. Finally, the early Miocene trench-fill clastic sediments date the arrival of the Palawan Continental Terrane in the trench along the Cagayan arc (Steuer et al., 2013; Aurelio et al., 2014; Suggate et al., 2014; Shao et al., 2017; Cao et al., 2021b).

Sarawak exposes OPS-mélange with blocks of Upper Jurassic to Upper Cretaceous radiolarian chert and Cretaceous trench-fill clastics (e.g., Jasin, 2000). U–Pb zircon detrital zircon geochronology on the trench-fill sediments revealed maximum depositional ages between 119 Ma and 88 Ma (Wang et al., 2021; Zhao et al., 2021). Similar mélange complexes are also present in northern Sabah, where they comprise gabbro, plagiogranite, pillow basalt, Cretaceous radiolarian chert, and trench-fill clastics (Jasin, 2000, 2018). Zircon U-Pb dating of gabbro samples from these North Borneo accretionary complexes, of which the (tectono-)stratigraphic context is not well known, yielded mean ages between 112 ± 2 Ma and 123 ± 1 Ma and basalt samples yielded $^{40}Ar/^{39}Ar$ plateau ages of ∼134.5 ± 2.8 Ma and 135.9 ± 2.2 Ma (Wang et al., 2023). Trench-fill sandstones yielded maximum depositional ages of ∼114 Ma, based on detrital zircon geochronology (Wang et al., 2023). The OPS mélanges in North Borneo are unconformably overlain by middle Eocene sandstones (Hutchison, 1996; Hutchison et al., 2000; Jasin and Tongkul, 2013; Van Hattum et al., 2013; Rahim et al., 2017) that farther to the north were incorporated into a north-vergent fold-thrust belt known as the Rajang-Crocker accretionary prism that formed during southward subduction below north Borneo along-strike of Palawan (Van Hattum et al., 2006, 2013; Lambiase et al., 2008).

2.2.2. OPS records of the Proto-South China Sea

Information about the Proto-South China Sea, which is the oceanic lithosphere that was preserved after Mesozoic subduction cessation, comes from the OPS sequence exposed in Palawan. These sequences are found thrusted over the Palawan Continental terrane, and, in turn, are overthrusted by supra-subduction zone ophiolites with latest Eocene metamorphic soles showing that they accreted in a late Eocene and younger subduction zone before the arrival of the Palawan Continental Terrane in the trench (Schlüter et al., 1996; Aurelio et al., 2014; Dycoco et al., 2021). These ophiolites were interpreted to have formed by inversion of a mid-oceanic ridge (Keenan, 2016), but regional kinematic restoration makes it more likely that they formed in the forearc

of a subduction zone along the northern SW Borneo continental block, which includes the basement of the Cagayan arc (Advokaat and Van Hinsbergen, 2023). The thrust vergence of the accreted rock units of Palawan is northward, showing geological evidence for southward Proto-South China Sea subduction (Hall, 2002; Keenan, 2016). Based on seismic tomographic interpretations, Wu and Suppe (2018) suggested that also an Eo-Oligocene northward subduction zone may have existed within the Proto-South China Sea, but there is no evidence for this interpretation in the geological record.

The OPS sequences that are tectonically sandwiched between the Palawan Continental Terrane and the Palawan Ophiolite, are somewhat confusingly known as the 'Southern Palawan Ophiolite' (Gibaga et al., 2020; Dycoco et al., 2021), but are not associated with metamorphic sole rocks and are instead interpreted as off-scraped relics of a subducted, oceanic lithosphere. The Southern Palawan Ophiolite was assigned a Mesozoic age based on the presence of Early Cretaceous nannoplankton in calcareous red clay associated with pillow basalts (Muller, 1991) and Upper Cretaceous radiolarian cherts (Wolfart et al., 1986). In addition, float samples of gabbro and syenite, interpreted to have been derived from the Southern Palawan Ophiolite, yielded 100.7 ± 1.2 Ma and 103.0 ± 1.1 Ma zircon U-Pb ages (Dycoco et al., 2021). Whether these samples are derived from the gabbroic section of the South Palawan Ophiolite or from intrusions into it is unknown, but the obtained ages provide minimum ages of the oceanic lithosphere of the Proto-South China Sea (Dycoco et al., 2021), which thus must already have existed prior to the cessation of subduction at the south China Sea margin. This falsifies hypotheses that propose that the Proto-South China Sea represents a Paleocene back-arc basin (e.g., Zahirovic et al., 2014). The volcanic section and the gabbroic float samples of the South Palawan Ophiolite have an ocean island basalt geochemical affinity, while a mafic dike has an island arc signature (Gibaga et al., 2020; Dycoco et al., 2021). Peridotites of the South Palawan Ophiolite have signatures transitional between Mid-Ocean Ridge Basalt (MORB) and Island Arc Tholeiite (IAT) and are interpreted to have formed in a supra-subduction zone environment (Labis et al., 2021).

The Proto-South China Sea was also lost to oblique eastward subduction below northern Luzon (e.g., Hall, 2002) and fragments of its oceanic crust may be preserved in the Philippines (Yumul et al., 2020). In western Luzon, a highly sheared mélange with a serpentinite matrix and blocks of Lower Cretaceous radiolarian cherts is exposed to the west of the Zambalas Ophiolite, referred to as the West Luzon Shear Zone (Karig, 1983). A similar serpentinite-matrix mélange (the Dos Hermanos Mélange), with uppermost Jurassic to Lower Cretaceous radiolarian chert is exposed in the northwest of Luzon, in the Ilocos Norte region (Queaño et al., 2017). Geochemical signatures of the Dos Hermanos Mélange ultramafic and mafic rocks display MORB and island arc signatures and are interpreted to have formed in a supra-subduction setting (Pasco et al., 2019).

3. Methods, results, and interpretation

We collected samples from an OPS sequence in the Cretaceous accretionary prism of Sabah, north Borneo. This OPS section forms part of a series of rocks in NW Borneo that is sometimes referred to as the Chert-Spilite formation, a somewhat outdated term (see Jasin, 1991, Hutchison, 2005). We performed fieldwork at a well-exposed section along the Baliojong River, northeast of Kota Marudu (Figs. 2 and 3). The rocks in this section are the youngest known accreted OPS units prior to the Eocene and younger Rajang-Crocker accretionary prism, and are hence presumably youngest parts of the Mesozoic accretionary prism exposed in Bor-

neo. We studied five sequences of OPS (B2-B5) that are exposed in thrust fault-bounded, coherent stratigraphic sections comprising pillow basalts with overlying radiolarian chert and trench-fill turbidites consisting of fine- to coarse-grained sandstone (Jasin and Tongkul, 2013). In a few instances, the oldest part of the deep marine sediments consists of a rhythmic alternation between radiolarian chert and red siltstone. We documented five sections from fault-bounded thrust slices. Each section is overturned with dips typically between 25° and 50° (115°–140°), but with local variation due to folding. In sections 2 and 3, the trench-fill clastic sediments were truncated from the OPS sequence along footwall cutoffs. Based on field relationships, it was not possible to conclusively demonstrate whether all thrust slices represent a duplexed series of a single accreted OPS sequence, or whether there are multiple OPS sections that accreted at different times. From four sections (B2–B5) we collected samples for geochemical analyses from pillow lavas, for radiolarian stratigraphy from chert sections, for paleomagnetic analyses from both pillow lavas and red clays intercalated in the basal chert sections, and finally, from two sections (B2 and B5) we collected turbiditic sandstones for sediment provenance and maximum depositional age analysis. Below, we describe the results and first-order interpretation per data type.

3.1. Basalts: Major and trace element geochemistry

3.1.1. Sampling and methods

We collected 22 samples of basaltic pillow lavas from sections 2, 3, 4, and 5 (See Fig. 2 for locations). Samples were crushed using a steel jaw crusher and ground in a tungsten carbide mill. Loss on ignition (LOI) was measured at 1000 °C by thermo-gravimetric analysis. Fusion beads were prepared for whole rock x-ray fluorescence (XRF) major element analysis using 0.6 g sample and 6 g of flux consisting of 66% lithium tetraborate, 34% lithium metaborate

and 0.5% lithium iodide. Wavelength dispersive XRF measurements for major elements were done sequentially with a Thermo Scientific ARL Perform'X 4200 W instrument at Utrecht University, the Netherlands. Results were reported on a loss-free basis.

Trace elements were measured by laser ablation inductively coupled plasma-mass spectrometry (LA-ICP-MS) on the fusion beads using a GeoLas 200Q 193 nm ArF Excimer laser ablation system coupled to a Thermo Finnigan Element2 sector field ICP-MS at Utrecht University. Fusion beads were ablated with a fluence of 12 J·cm^{-2}, a pulse repetition rate of 10 Hz and with a crater diameter of 120 µm. Calibration was performed against NIST SRM 612 glass using standard data reduction protocols (Longerich et al., 1996) and accuracy was monitored using the USGS basaltic glass standard BCR2-G.

Three basaltic standard reference materials, BIR-1, JB-1B and JB-2 were treated as external standards and were measured in parallel with the basaltic rocks collected in this study. Results are reported alongside the samples in Table 1 and show excellent agreement with recommended values from the GEOREM database (Jochum et al., 2005), to within 10% of recommended values for most elements measured.

3.1.2. Results and interpretation

Eighteen samples plot as basalts on the total alkali-silica diagram (Le Bas et al., 1986) and four have slightly elevated SiO_2, plotting in the basaltic andesite field. Major elements such as MgO, Al_2O_3 and CaO vary across this range in SiO_2 consistent with minor degrees of fractional crystallization (Table 1). Loss on ignition was typically below 5%, but some samples showed elevated LOI and/or an increase Na_2O and K_2O that reflects minor post-magmatic alteration (Table 1). Increased concentrations of alkalis compromise the use of these elements in tectonic discrimination diagrams. In contrast, immobile trace element ratios and relative abundances are
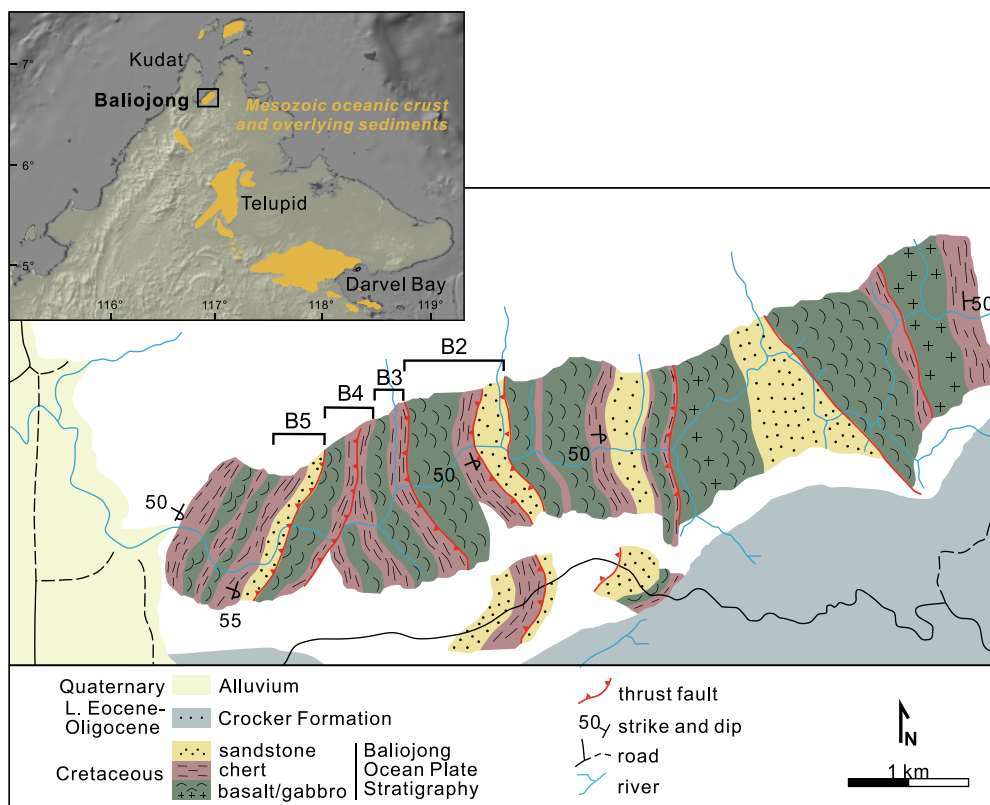

Fig. 2. Geological map of the OPS sections of the Baliojong River showing the sampled sections (based on Jasin and Tongkul, 2013). Inset: Generalized geological map of Sabah, showing the distribution of Mesozoic ophiolite and OPS exposures.

Fig. 3. Field photos from the Baliojong River OPS: (A) Sandstone turbidite; (B) Overturned contact (highlighted with yellow line) between pillow basalts and radiolarian cherts; (C) Rhythmic alternation between radiolarian chert and red cherty siltstone; (D) Pillow basalts. (For interpretation of the references to colour in this figure legend, the reader is referred to the web version of this article.)

consistent with a mid-ocean ridge basalt (MORB) origin, for example using Zr vs Ti, Ti/Y vs Zr/Y and Ti/1000 vs V (Supplementary Data Fig. S1; Rollinson et al., 2021). Rare earth element abundances further constrain the tectonic setting and are consistent with a slightly enriched E-MORB origin, with Ce/Yb$_N$ equal to or > 1 (Supplementary Data Fig. S2).

Samples from the four thrust sheets show distinctive trace element compositions with variable degrees of enrichment seen between the sampled locations, reflecting variable degrees of input from N-MORB and E-MORB mantle sources. This is shown most clearly on a plot of Th/Yb vs Nb/Yb where variable enrichment is seen around average E-MORB (Fig. 4; Pearce, 2008). There is no evidence for fluid-modified melting or melting of more enriched OIB mantle sources in the source of the basalts that we sampled. In summary, the basalts were produced by melting of an enriched MORB source, coupled with minor degrees of fractional crystallization. These data would be consistent with an origin in an oceanic plateau, although a mid-oceanic ridge setting is not excluded.

3.2. Radiolarian cherts: Biostratigraphy

3.2.1. Sampling and methods

We collected 29 samples of radiolarian chert and red cherty siltstone from the Baliojong River OPS, nine samples from section BC2, ten samples from section BC3, and ten samples from section BC5, to complement earlier biostratigraphic results for the Baliojong River section of Jasin and Tongkul (2013). All samples were crushed into small fragments (1 cm to 2 cm), which were subsequently dissolved using dilute hydrofluoric acid 5% and water, with a ratio of acid to water of 1:9 and soaked for about 24 h (the concentration of acid and the time of treatment varied slightly,

depending on the sample) (Pessagno and Newport, 1972). After that all samples were rinsed with fresh water and dried before they were examined under the microscope. Well-preserved specimens were photographed using scanning electron microscopy (SEM) for further examination.

3.2.2. Results and interpretation

The classification, taxonomy and biostratigraphic range of the radiolarian species are based on Sanfilippo and Riedel (1985), Thurow (1988), Vishnevskaya (1993) and O'Dogherty (1994). All samples collected contain radiolarian skeletons that are moderately to well-preserved. The amount of radiolarian skeletons in the red siltstone samples was much lower than in the radiolarian chert samples. We identified a total of 62 radiolarian species and some selected radiolarian species are portrayed in Supplementary Data Fig. S3.

The biostratigraphic analysis of the radiolarian species, which is described in detail in Supplementary Data Text 1 and Table S1, reveals two assemblages of radiolarian species that are identified in all three sections (Fig. 5). Assemblage I ranges in age from Barremian to Aptian (Early Cretaceous, i.e., 126.5–113.2 Ma) and is represented by samples BC2.9 to BC2.5 in Section BC2, samples BC3.10 to BC3.4 in section B3 and samples BC5.10 to BC5.3 in Section BC5. Assemblage II is indicative of Albian to Cenomanian age (Early to Late Cretaceous, i.e. 113.2–93.9 Ma) and is recorded in samples BC2.4 to BC2.1 in section BC2, samples BC3.3 to BC3.1 in section B3 and sample BC5.2 and BC5.1 in section BC5. This confirms previous biostratigraphic results of Jasin and Tongkul (2013) and shows that the E-MORB basalts of the Baliojong River section formed in Early Cretaceous times, and must have formed on an ocean floor that predated this age.

Table 1
Major and trace element compositions of the Baliojong River basalt samples.

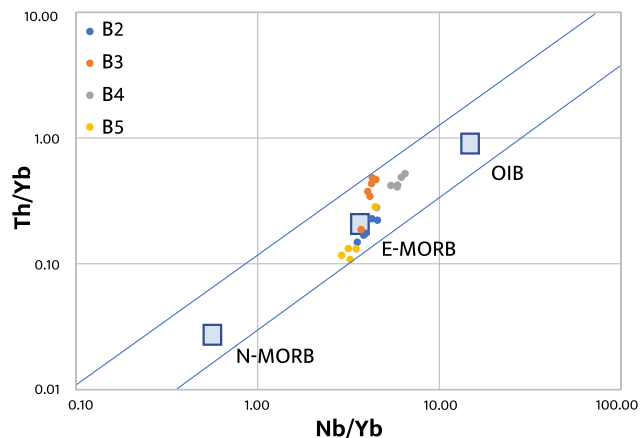| wt.%	PB 2.1	PB 2.8	PB 2.13	PB 2.35	PB 2.50	PB 3.15	PB 3.26	PB 3.4	PB 3.5	PB 3.6	PB 3.44	PB 4.7	PB 4.21	PB 4.23	PB 4.24	PB 4.38	PB 4.48	BB 5.1	BB 5.2	BB 5.3	BB 5.4	BB 5.5	BIR-1	JB-1B	JB-2
SiO_2	49.87	53.59	49.06	52.24	50.62	50.12	48.75	52.89	50.87	51.03	49.77	51.82	53.82	50.75	48.39	49.34	52.98	49.88	49.60	45.72	47.58	50.72	46.78	51.51	52.32
Al_2O_3	17.00	14.95	16.45	14.84	15.70	16.70	16.88	16.38	17.34	17.50	18.09	15.38	15.46	15.78	15.43	16.33	13.87	16.55	15.86	14.44	16.01	15.27	15.57	14.59	14.73
TFe_2O_3	8.24	9.33	10.36	10.19	9.94	9.00	9.65	7.95	7.79	7.65	8.10	9.73	8.42	10.60	13.23	9.16	9.70	9.96	10.10	10.42	10.57	9.12	11.42	9.08	14.35
MnO	0.13	0.15	0.17	0.17	0.16	0.13	0.15	0.15	0.17	0.17	0.17	0.16	0.14	0.17	0.17	0.20	0.17	1.08	0.15	0.17	0.22	0.17	0.18	0.15	0.22
MgO	6.72	7.78	6.21	8.86	6.94	7.53	6.84	8.49	8.82	8.65	9.04	7.84	7.07	7.91	6.91	7.16	7.72	7.37	6.32	6.36	6.25	7.57	9.55	8.48	4.60
CaO	11.92	6.39	10.84	7.07	8.81	8.56	11.05	6.01	7.65	7.49	8.86	7.27	6.31	6.66	8.08	9.45	8.10	8.03	10.59	16.33	13.63	10.20	13.11	9.52	9.61
Na_2O	2.81	4.67	4.70	3.65	3.46	2.68	2.75	5.27	4.08	3.94	2.66	4.33	3.98	3.42	2.92	2.67	2.51	4.00	3.34	2.51	3.53	3.45	1.71	2.59	1.92
K_2O	0.99	0.62	0.14	0.66	1.87	2.78	1.43	0.43	0.94	1.13	0.88	1.06	1.62	1.94	2.05	2.67	2.07	0.61	1.76	1.89	0.45	1.33	0.01	1.32	0.41
TiO_2	1.23	1.53	1.14	1.70	1.32	1.24	1.14	1.14	1.16	1.21	1.19	1.51	2.04	1.83	1.76	1.83	1.85	1.57	1.14	0.97	1.17	1.10	0.90	1.19	1.10
P_2O_5	0.13	0.22	0.11	0.13	0.19	0.13	0.19	0.17	0.17	0.18	0.16	0.16	0.38	0.35	0.24	0.25	0.24	0.17	0.11	0.14	0.10	0.10	0.01	0.23	0.08
Total	99.04	99.23	99.18	99.51	99.01	98.87	98.83	98.88	98.99	98.95	98.92	99.26	99.24	99.41	99.18	99.06	99.21	99.22	98.97	98.95	99.51	99.03	99.24	98.66	99.34
LOI	2.92	3.00	4.42	3.66	3.84	3.92	5.87	3.56	3.99	3.85	3.74	2.87	3.18	3.65	3.75	4.77	3.10	7.59	3.73	7.53	5.20	3.00			
ppm																									
Sc	45.4	48.6	41.2	47.8	45.8	45.8	39.6	41.3	41.7	43.0	40.7	49.6	44.1	44.1	43.4	41	43.3	43.8	48	42.9	49.6	45	50	33	61
Ti	9628	12,042	8833	13,212	9970	9663	8830	8808	8982	9497	9473	11,983	15,983	14,328	13,832	14,137	13,980	11,995	8692	7430	8947	8389	7262	9100	8499
V	279	240	268	259	276	289	279	241	276	278	283	289	227	258	288	265	265	191	259	286	258	270	375	228	643
Cr	388	254	457	139	374	405	403	430	443	436	409	264	87	239	228	312	183	357	422	407	453	438	485	532	59
Mn	985	1180	1330	1263	1174	1001	1169	1152	1302	1326	1364	1256	1022	1276	1276	1441	1236	8174	1114	1290	1646	1257	1401	1119	1685
Co	66.1	44.1	61.7	64.3	52.7	57.7	60.7	73.0	64.4	80.9	84.2	65.8	47.4	52.8	49.0	52.0	60.3	46.3	47.0	47.2	49.5	51.0	58.3	41.0	37.0
Ni	118	65	112	70	75	98	143	200	180	202	188	76	57	60	53	107	90	112	76	73	80	75	189	174	30
Cu	41	60	85	44	70	48	67	67	65	66	65	67	39	42	35	24	28	51	419	32	170	73	88	41	179
Zn	107	108	113	108	82	98	91	88	95	81	98	113	95	112	106	107	69	102	90	76	85	75	86	88	117
Ga	18	13	17	14	21	25	18	14	18	17	19	14	17	19	22	20	17	21	27	28	17	24	15	28.9	20
As	2.1	2.8	4.4	2.3	2.1	1.6	3.7	2.9	2.1	2.6	1.7	3.9	2.4	4.0	3.3	3.0	3.8	5.3	1.3	1.4	1.5	1.3	2.1	1.7	2.2
Rb	14	11	2	12	30	28	13	5	9	12	9	21	17	27	35	27	19	21	31	28	9	25	0.26	39	6.4
Sr	179	141	116	135	178	116	115	201	242	243	172	135	167	158	135	192	119	169	199	197	153	249	113	451	179
Y	25	30	23	33	29	25	25	22	23	25	25	28	34	31	28	31	32	28	24	25	25	24	15	21	22
Zr	78	104	70	114	92	79	80	76	76	81	81	96	162	118	125	135	132	112	65	56	69	63	15	119	43
Nb	5.1	9.2	4.8	9.4	6.4	6.3	13.3	14.0	14.1	14.2	12.2	9.7	21.9	14.8	15.6	16.5	16.2	11.0	4.3	3.4	4.6	4.3	0.6	25.6	0.6
Mo	1.3	1.8	1.6	1.6	2.2	2.0	1.8	2.1	2.6	1.6	1.3	1.6	1.8	1.8	1.5	1.6	1.3	1.8	6.0	2.3	2.9	1.5	1.3	6.0	2.1
Cs	0.71	0.32	0.06	0.29	1.15	1.14	0.40	0.19	0.51	0.78	0.49	0.70	0.49	0.92	1.30	0.96	0.51	0.93	1.43	1.92	0.25	2.20	0.02	0.84	0.80
Ba	92	83	64	66	282	389	151	140	227	217	175	70	113	141	144	153	113	240	466	495	182	443	9	540	219
La	4.8	8.5	4.7	7.0	6.7	5.8	8.9	7.0	8.1	8.1	7.6	8.1	18.0	14.4	12.7	12.7	11.8	8.7	4.3	5.1	4.2	4.2	0.6	40.4	2.3
Ce	12.6	20.0	11.2	16.5	15.6	13.6	18.9	15.9	17.8	18.4	17.5	19.2	38.2	31.7	28.1	28.6	26.4	20.3	11.3	10.0	10.4	10.8	1.6	70.0	6.5
Pr	1.77	2.80	1.60	2.70	2.29	1.94	2.38	2.24	2.28	2.40	2.30	2.70	4.82	4.00	3.57	3.64	3.60	2.72	1.47	1.68	1.56	1.49	0.39	7.20	1.10
Nd	9.5	14.1	8.5	14.3	11.6	9.7	11.1	9.5	10.7	11.2	11.0	12.4	21.9	18.2	16.7	17.2	17.5	13.4	8.2	8.4	8.2	8.5	2.8	26.1	6.1
Sm	3.1	3.9	2.6	4.3	3.4	2.9	2.9	2.9	3.1	2.9	3.2	3.9	5.5	4.8	4.2	4.4	4.6	3.7	2.9	2.7	2.5	2.7	1.1	5.2	2.1
Eu	1.2	1.3	1.1	1.4	1.2	1.1	1.1	0.9	1.0	1.1	1.1	1.1	1.8	1.6	1.5	1.6	1.6	1.3	1.0	1.1	1.0	1.2	0.5	1.5	0.7
Gd	3.90	4.70	3.51	5.50	4.29	4.00	3.80	3.50	3.50	3.60	3.98	4.40	6.10	5.40	4.80	4.90	5.40	4.20	3.90	3.49	3.80	3.50	1.85	4.40	2.90
Tb	0.63	0.81	0.62	0.87	0.73	0.64	0.58	0.58	0.60	0.61	0.62	0.75	0.96	0.85	0.80	0.87	0.86	0.70	0.61	0.61	0.64	0.61	0.34	0.60	0.46
Dy	4.6	5.4	4.1	6.2	5.2	4.6	4.5	3.9	4.0	4.6	4.4	5.1	6.2	5.7	5.4	5.5	5.9	5.0	4.2	4.4	4.6	4.4	2.6	4.1	3.8
Ho	0.96	1.14	0.81	1.22	1.04	0.95	0.89	0.82	0.86	0.93	0.90	1.03	1.26	1.15	1.05	1.14	1.23	1.07	0.90	0.90	0.99	0.95	0.56	0.76	0.81
Er	2.77	3.19	2.43	3.43	3.10	2.68	2.51	2.41	2.46	2.73	2.77	3.10	3.52	3.18	2.98	3.28	3.20	3.20	2.80	2.56	2.69	2.60	1.76	2.10	2.40
Yb	2.70	3.08	2.20	3.36	2.95	2.60	2.75	2.20	2.40	2.60	2.64	2.70	3.40	3.10	2.71	3.18	2.97	3.00	2.40	2.60	2.81	2.70	1.68	1.90	2.90
Lu	0.35	0.43	0.32	0.46	0.44	0.39	0.37	0.34	0.35	0.41	0.38	0.43	0.48	0.44	0.41	0.46	0.44	0.47	0.40	0.37	0.40	0.40	0.26	0.27	0.33
Hf	2.00	2.60	1.80	2.73	2.29	2.13	2.05	1.86	1.83	2.10	2.05	2.60	4.05	3.00	2.92	3.20	3.21	2.90	1.90	1.58	1.82	1.70	0.60	3.00	1.40
Ta	0.77	1.04	0.70	0.96	0.82	0.88	1.27	1.31	1.24	1.33	1.15	1.10	1.82	1.47	1.38	1.43	1.41	1.19	0.80	0.73	0.80	0.72	0.05	1.90	0.48
Pb	0.80	1.01	0.73	1.40	1.44	0.70	0.84	0.56	0.68	1.90	0.39	0.80	1.40	1.14	1.10	1.18	1.11	3.30	0.90	0.67	1.20	0.80	3.60	5.30	4.30
Th	0.40	0.68	0.37	0.77	0.51	0.49	1.03	1.07	1.12	1.14	0.91	0.77	1.76	1.26	1.32	1.33	1.26	0.85	0.31	0.28	0.33	0.35	0.04	8.90	0.24
U	0.18	0.39	0.16	0.35	0.14	0.15	0.49	0.40	0.31	0.60	0.25	1.30	0.50	0.47	0.38	0.60	0.60	0.16	0.50	0.10	0.17	0.20	0.02	1.30	0.17

Fig. 4. Th/Yb versus Nb/Yb diagram of the Baliojong River pillow basalt samples. Geochemical discrimination based on Pearce (2008).

3.3. Foreland basin clastics: Detrital zircon geochronology and provenance

3.3.1. Sampling and methods

We collected a total of twelve samples from turbiditic sandstones: seven samples (BF2.1 to BF2.7) from section B2, and five samples (BF5.1 to BF5.5) from section B5; sections B3 and B4 do not contain sandstone. As shown in representative thin section photomicrographs (Supplementary Data Fig. S4), samples of section BF2 are quartzose sandstones composed of angular to subangular quartz with feldspar, sericite, and chert clast, whereas those of section BF5 are calcite-bearing lithic arenites. These samples were prepared for whole-rock geochemical analysis, heavy mineral analysis and detrital zircon single-grain geochronology using procedures described in Supplementary Data Text 2.

3.3.2. Results

3.3.2.1. Whole-rock geochemistry. The results of major and trace element analyses of the sandstone samples are provided in Table 2. In the ternary diagram of relative proportions of Ca, Al, and Si (Fig. 6A), samples of section BF2 plot near the Si apex, showing dominance of detrital silicates therein. In contrast, samples of section BF5 are separate from this cluster due to a varying degree of Ca dilution (31.8% – 0.8%), which correlates with authigenic components therein. This compositional difference is also observed in the Upper Continental Crust (UCC; Rudnick and Gao, 2014)-normalized elemental distributions (Fig. 6B). Samples of section BF2 display slight enrichment of Mn, Zr, and Hf and strong depletion of Ca and Na, whereas strong enrichment of Ca and Mn and slight depletion of Zr and Hf in samples of section BF5 confirm the dilution by authigenic components. In addition, samples of the two sections show a varying degree of depletion of large-ion lithophile elements (e.g., K, Rb, Sr, Cs, and Ba) and high field-strength elements (e.g., Nb, Th, and U). In the distribution of chondrite-normalized (Sun and McDonough, 1989) rare earth
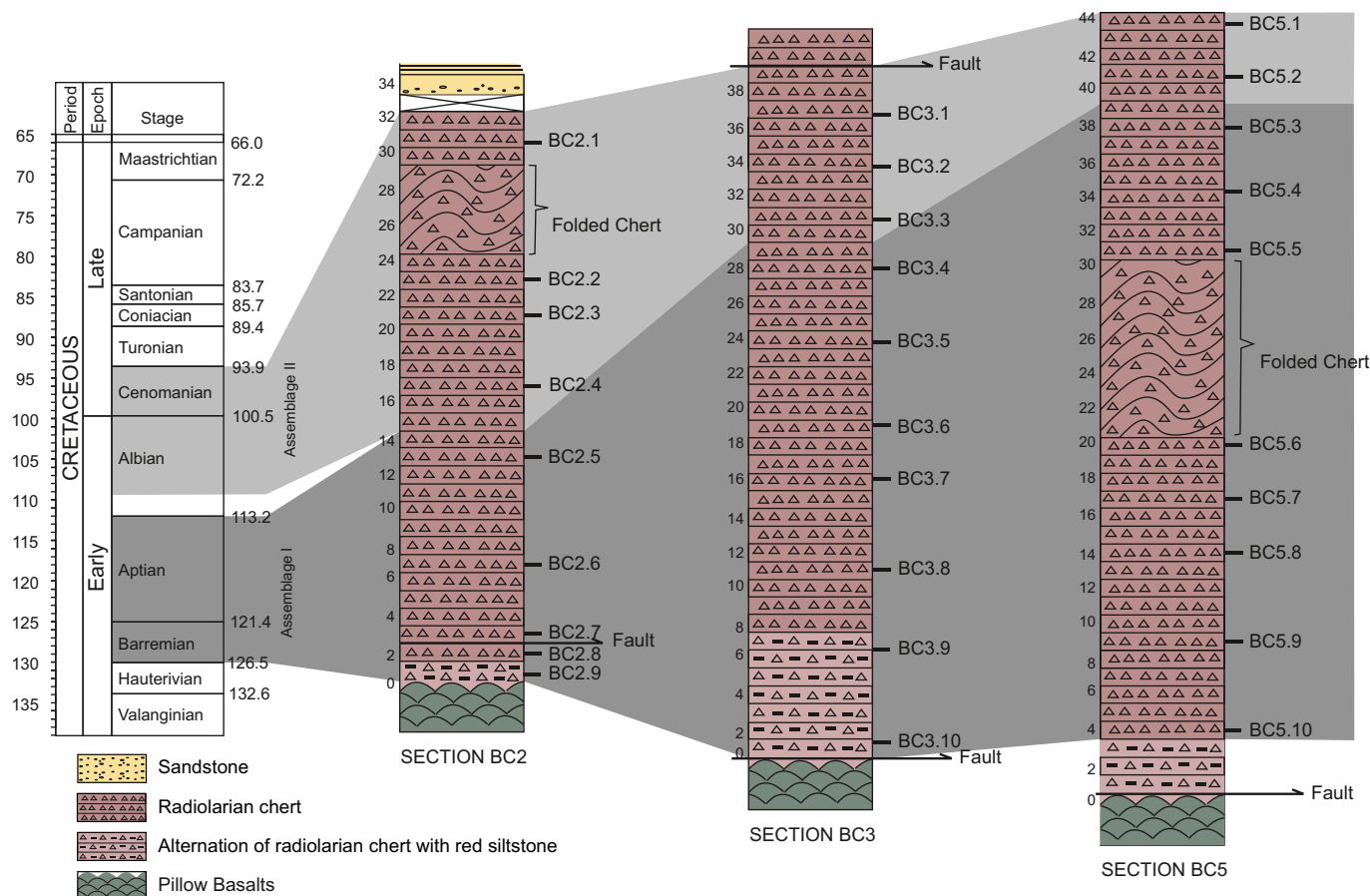

Fig. 5. Correlations of radiolarian biostratigraphy in sections BC2, BC3, and BC5. Section length in meters. Time scale based on Gradstein et al. (2020).

Table 2
Major and trace element compositions of Baliojong River sandstone samples.

wt.%	BF2.1	BF2.2	BF2.3	BF2.4	BF2.5	BF2.6	BF2.7	BF5.1	BF5.2	BF5.3	BF5.4	BF5.5
SiO_2	81.10	75.94	79.69	88.01	81.01	85.57	84.16	44.40	68.18	35.35	31.05	29.67
TiO_2	0.37	0.54	0.45	0.25	0.45	0.19	0.41	0.49	0.73	0.47	0.39	0.42
Al_2O_3	6.68	9.44	7.82	4.14	7.11	3.26	7.14	10.92	14.64	10.35	9.16	9.62
TFe_2O_3	4.73	3.22	2.84	2.72	3.18	1.72	2.62	9.59	5.20	4.75	4.27	4.43
MnO	0.26	0.18	0.13	0.18	0.19	0.47	0.10	1.02	0.22	2.85	2.60	3.49
MgO	0.91	1.09	0.92	0.51	1.06	0.51	0.66	2.65	2.15	2.20	1.85	2.03
CaO	0.78	2.13	2.16	1.07	1.36	3.15	0.21	14.04	0.73	20.15	24.65	23.54
Na_2O	0.77	1.05	0.07	0.38	1.04	0.47	1.10	0.44	1.00	2.56	2.70	2.43
K_2O	0.96	1.53	1.05	0.53	0.97	0.44	1.00	1.09	2.34	0.65	0.45	0.55
P_2O_5	0.07	0.08	0.08	0.04	0.06	0.03	0.06	0.50	0.08	0.82	0.31	0.25
Total	96.63	95.20	95.21	97.83	96.43	95.81	97.46	85.14	95.27	80.15	77.43	76.43
LOI	2.91	4.43	4.70	1.59	3.04	3.45	2.05	14.45	4.25	19.36	21.80	23.53
ppm												
Li	31.63	34.03	30.62	15.37	25.36	14.48	27.90	57.56	50.41	26.40	21.83	21.34
Be	0.69	1.31	0.87	0.51	0.87	0.50	0.89	1.29	1.71	0.81	0.61	0.62
Sc	4.97	7.08	5.57	3.12	5.41	2.22	5.35	10.28	12.36	15.02	12.26	13.76
V	47.36	56.48	44.49	33.26	44.52	19.03	48.96	87.96	156.99	105.65	85.72	91.39
Cr	1605.91	336.16	498.66	1696.31	636.57	458.78	503.95	82.36	186.99	105.70	33.79	188.08
Co	23.83	12.01	10.48	20.99	12.68	9.78	15.59	15.05	21.29	13.53	12.96	11.37
Ni	672.82	143.00	215.13	678.91	266.17	170.58	212.30	67.90	97.52	67.59	33.67	103.83
Cu	63.08	28.84	26.21	87.14	39.41	28.31	41.65	79.20	98.40	76.55	75.67	48.86
Zn	47.70	54.91	44.03	28.77	36.84	23.70	42.74	124.79	91.65	58.19	50.03	53.95
Ga	7.68	11.15	8.63	4.84	8.48	4.10	8.25	13.05	17.31	11.31	9.63	10.93
Rb	35.71	61.83	46.14	22.21	42.64	19.16	41.81	51.65	106.41	24.46	16.32	21.46
Sr	30.46	46.19	39.87	27.77	48.59	40.57	41.30	112.35	71.67	115.95	107.54	108.18
Y	18.14	22.48	16.81	12.10	19.83	11.79	17.46	40.02	25.36	39.90	33.04	41.63
Zr	312.92	236.57	245.56	288.62	396.18	270.74	372.87	98.91	189.16	74.67	60.88	67.86
Nb	6.88	9.85	8.31	5.03	8.35	4.16	7.68	6.90	11.78	2.28	1.76	1.92
Sn	1.98	1.83	1.55	1.66	1.67	1.00	1.63	1.47	2.42	0.89	0.63	0.75
Cs	1.72	3.34	2.47	1.13	2.25	1.10	2.19	3.61	7.24	1.52	1.17	1.50
Ba	206.06	134.12	112.37	79.56	85.53	103.14	101.37	130.02	253.20	384.80	270.48	336.21
La	19.19	22.95	17.08	11.85	20.46	12.65	20.16	40.75	22.24	20.14	13.19	14.17
Ce	38.74	45.84	35.70	24.37	40.58	26.28	40.87	87.98	45.52	39.19	25.07	27.94
Pr	4.60	5.43	4.19	2.89	4.72	3.01	4.55	11.56	5.26	5.60	3.60	4.09
Nd	18.06	20.65	15.71	10.87	17.49	11.44	16.65	52.68	20.23	26.08	16.41	19.18
Sm	3.90	4.35	3.04	2.31	3.26	2.29	3.00	13.14	4.36	6.45	4.20	5.11
Eu	0.76	0.92	0.65	0.45	0.70	0.46	0.57	2.94	0.90	1.65	1.17	1.49
Gd	3.52	4.08	3.05	2.23	3.14	2.11	2.67	12.64	4.09	7.21	4.97	6.08
Tb	0.51	0.66	0.49	0.35	0.53	0.34	0.45	1.72	0.70	1.12	0.81	1.02
Dy	3.17	3.78	2.90	2.03	3.25	1.91	3.04	8.48	4.40	6.33	5.20	6.54
Ho	0.65	0.76	0.62	0.41	0.68	0.38	0.63	1.39	0.90	1.27	1.06	1.30
Er	1.87	2.30	1.76	1.22	2.02	1.19	1.96	3.43	2.78	3.56	3.27	3.94
Tm	0.29	0.34	0.27	0.20	0.31	0.18	0.31	0.44	0.41	0.51	0.48	0.57
Yb	1.83	2.19	1.82	1.28	2.08	1.20	2.08	2.68	2.66	3.24	2.98	3.66
Lu	0.28	0.33	0.27	0.21	0.33	0.19	0.33	0.39	0.40	0.48	0.46	0.56
Hf	8.08	6.38	6.32	7.28	10.12	7.01	9.62	2.86	5.20	2.24	1.74	2.03
Ta	0.55	0.74	0.64	0.36	0.65	0.34	0.61	0.51	0.91	0.18	0.12	0.14
Tl	0.34	0.56	0.31	0.16	0.28	0.17	0.60	0.31	1.06	0.18	0.16	0.18
Pb	11.88	9.94	5.60	9.92	9.88	15.89	18.06	25.21	61.15	8.46	24.78	4.90
Th	7.24	8.53	7.10	4.52	8.17	4.21	7.93	6.53	11.43	2.25	1.74	1.84
U	2.04	2.26	2.03	1.68	2.42	1.51	2.65	2.56	4.36	1.20	1.02	0.67

elements (REE), samples of the two sections are comparable in showing moderate light-REE enrichment and negative Eu anomalies, with average $\sum LREE/\sum HREE$ and δEu $((Eu/\sqrt{Sm*Gd})_N)$ values of 6.1 and 0.7, respectively (Fig. 6C). The REE concentrations of section BF5 (average 131.3 ppm), because of relatively enriched middle and heavy-REEs, are systematically higher than those of section BF2 (average 88.7 ppm), which could be caused by the preferential adsorption of REEs in more fined-grained sediments of section BF5. Among all samples, sample BF5.1 features the largest REE concentration (240.2 ppm) and strong light-REE enrichment relative to heavy-REE with a $(La/Lu)_N$ ratio of 11.1.

Geochemical data are also plotted in different diagrams for compositional discrimination (Fig. 6D-G). The Hf-La/Th and Zr/Sc-Th/Sc plots show increasing old components and corresponding sediment recycling for samples of section BF2 (Fig. 6D-6E), which is consistent with their slight Hf and Zr enrichment observed in the UCC-normalized curves (Fig. 6B). In contrast, most samples of

section BF5 have a geochemical affinity of an andesitic arc source with limited influence of sediment recycling. Samples between sections BF2 and BF5 are further discriminated by ferromagnesian elements with the former and the latter plotting towards more mafic and felsic source endmembers, respectively (Fig. 6F-G). Likewise, Cr and Ni in samples of section BF2, compared to UCC, are highly enriched by a factor of up to 17.5 and 14.3, respectively (Fig. 6B). The major element-based discriminant function diagram (Roser and Korsch, 1988) does not perform well in provenance discrimination and samples show a scattered distribution between the fields of mafic and intermediate sources (Fig. 6F).

3.3.2.2. Heavy minerals. Samples of sections BF2 and BF5 show great difference in heavy mineral compositions (Fig. 7, Table 3). The mineral assemblages in section BF2 are consistent, with dominant zircon (average 50.6%) and pyrite (average 23.3%) as well as a minor percentage of rutile, Cr-spinel, and leucoxene. Sample BF2.7
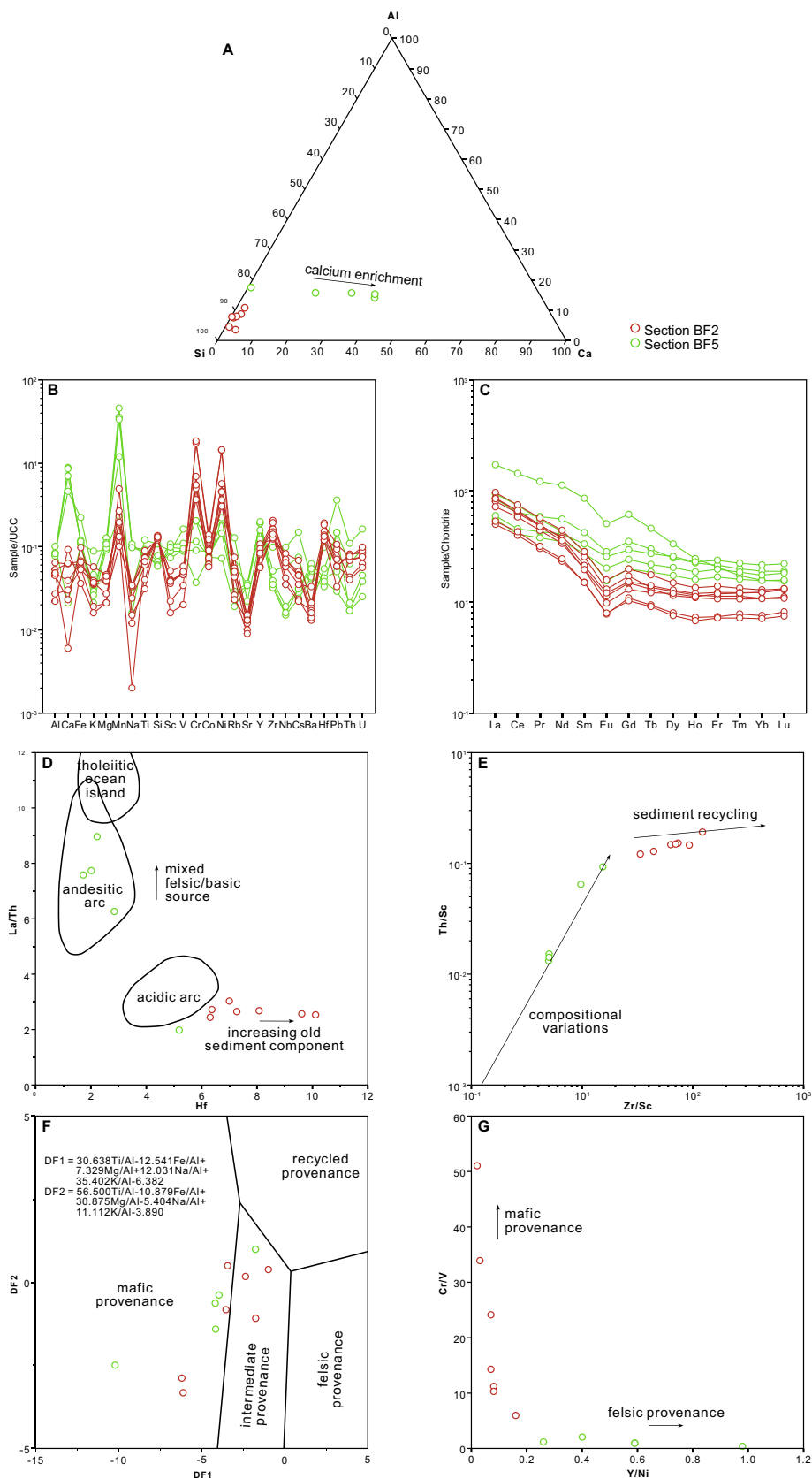
Fig. 6. Geochemistry of sandstone samples. (A) Ternary diagram showing the relative concentrations of Ca, Al, and Si of Baliojong sandstone samples. The sum of three components is normalized to 100 (wt.%); (B–C) Major and trace element and REE spider diagrams, normalized to Upper Continental Crust (UCC; Rudnick and Gao, 2014) and Chondrite (Sun and McDonough, 1989), respectively. (D–G) Element-based provenance discrimination diagrams of Baliojong sandstone samples. (D) Hf versus La/Th plot (Floyd and Leveridge, 1987). (E) Zr/Sc versus Th/Sc plot (McLennan et al., 1993). (F) Discriminant function diagram of major elements (Roser and Korsch, 1988). (G) Y/Ni versus Cr/V plot (McLennan et al., 1993).
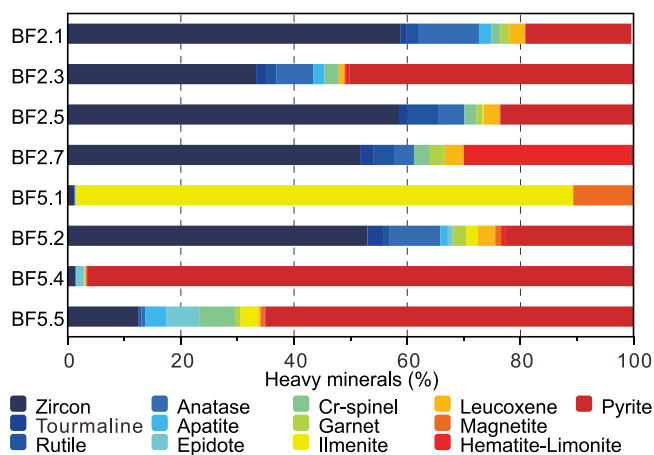
Fig. 7. Relative abundance of heavy minerals of Baliojong sandstone samples.

also contains abundant hematite-limonite. In contrast, the mineral compositions significantly vary in section BF5. While the mineral assemblage of sample BF5.2 is comparable to that of section BF2, sample BF5.1 and samples BF5.4 and BF5.5 are dominated by ilmenite (87.8%) and pyrite (average 80.1%), respectively. Compared to the moderate to high percentage of stable minerals (including zircon, tourmaline, and rutile) in section BF2, the commonly lower values in section BF5 suggest lower compositional maturity due to the lack of detrital components therein.

3.3.2.3. Detrital zircon geochronology. A total of 640 zircon grains from sections BF2 and BF5 were analyzed in this study. The results of zircon single-grain analyses of sandstone samples, including U-Pb geochronology, geochemistry, grain size and shape, are provided in Supplementary Data Table S2. Detrital zircon age signals within each section show a varying degree of inter-sample variation (Fig. 8). In section BF2, samples BF2.3 and BF2.5 consistently show strong age peaks at ca. 115 Ma and 240–235 Ma, a subordinate peak at ca. 450–430 Ma, as well as a scattered distribution of Proterozoic ages. The age signals of samples BF2.1 and BF2.7 are slightly different from the above pattern, with a larger percentage of Cretaceous ages and fewer Proterozoic ages in the former and an implicit peak of Ordovician-Silurian (i.e., mid-Paleozoic) ages in the latter. Greater inter-sample variety of age signals is observed in section BF5. Samples BF5.2 and BF5.5 feature a near unimodal signal with dominance of Jurassic–Cretaceous ages and a scattered distribution of more ancient ages. The Jurassic cluster peaking at ca. 150 Ma is also seen in sample BF5.4, albeit with subordinate peaks at ca. 225 Ma, 435 Ma, and 1840 Ma. In contrast, sample BF5.1 features an Early Cretaceous cluster peaking at ca. 120 Ma and a weak Caledonian peak. Samples within each section are

grouped to characterize their overall age signals. Along with the common occurrence of the Caledonian cluster and scattered Proterozoic ages, sections BF2 and BF5 are clearly discriminated by a moderate lull and a strong peak of Jurassic ages, respectively.

3.3.3. Interpretation

The radiolarian biostratigraphic ages of the Baliojong OPS reveal that the foreland basin clastics are younger than Albian–Cenomanian (Jasin and Tongkul, 2013; see section 3.2). We use the U-Pb detrital zircon ages to establish the maximum depositional age of the foreland basin clastics (Dickinson and Gehrels, 2009), which in accretionary orogens adjacent to active arcs are typically close to the depositional age (Cawood et al., 2012).

We calculate maximum depositional ages using eight proxies: (i) the youngest single grain age (YSG); (ii) the 'youngest detrital zircon' age calculated by Isoplot (YDG; Ludwig, 2003); (iii) the maximum likelihood age calculated by IsoplotR (MLA; Vermeesch, 2021); (iv) the weighted mean age of three youngest grains (YG(3); Zhang et al., 2015); (v) the weighted mean age of the youngest cluster with two or more grains overlapping in age at 1σ (YGC1σ(2 +); Dickinson and Gehrels, 2009); (vi) the weighted mean age of the youngest cluster with three or more grains overlapping in age at 2σ (YGC2σ(3 +); Dickinson and Gehrels, 2009); (vii) the weighted mean age of the youngest cluster with a mean square weighted deviation (MSWD) of ~1 (YSP; Coutts et al., 2019); (viii) the youngest graphic peak age of the kernel density estimation (KDE) spectrum (YPP).

Among 640 zircon grains analyzed in this study, two concordant grains (BF2.5–45 and BF5.5–45) are dated with Eocene ages (36.6 Ma and 41.6 Ma) with one containing a very high U concentration of 3056.3 ppm (Supplementary Data Table S2). The rare existence of these abnormally young ages contrasts with the ages of the unconformably overlying Crocker Formation and cannot represent the sedimentary age of the foreland basin clastics (Jasin and Tongkul, 2013; Hall and Breitfeld, 2017). Moreover, the Crocker formation has a distinctly different geochronological signal in the absence of Neoproterozoic and Ordovician–Silurian zircons (Supplementary Data Fig. S5). We infer that these Eocene grains may potentially be influenced by Pb loss, and we excluded them in the calculation of maximum depositional ages.

Different proxies of maximum depositional ages of sandstone samples range from 109.0 Ma to 79.9 Ma in section BF2 and from 114.0 Ma to 86.3 Ma in section BF5, but they do not explicitly show a younging or aging trend within each section (Fig. 9). Age proxies roughly cluster in samples BF2.1, BF5.2, and BF5.5 and the age estimates through the YSG, YDG, and MLA approaches are younger than the other proxies.

Following the data treatment strategy of Rinke-Hardekopf et al. (2021), regardless of the choice of age proxies, the calculated maximum depositional ages mostly belong to the Late Cretaceous and individual age proxies of section BF2 are about 6 Ma younger than those of section BF5. The interpretation of different depositional

Table 3
Relative abundance of heavy minerals and zircon-tourmaline-rutile.

| Sample	Zircon	Tourmaline	Rutile	Anatase	Apatite	Epidote	Cr-spinel	Garnet	Ilmenite	Leucoxene	Magnetite	Hematite-Limonite	Pyrite
BF2.1	58.86	0.94	2.11	10.77	2.24	0.00	1.59	1.54	0.00	2.75	0.04	0.09	18.70
BF2.3	33.29	1.91	1.64	6.61	1.90	0.01	2.54	0.04	0.00	0.93	0.17	0.72	50.24
BF2.5	58.55	1.57	5.47	4.49	0.10	0.00	2.04	1.10	0.18	2.80	0.09	0.10	23.50
BF2.7	51.67	2.43	3.57	3.52	0.00	0.00	2.82	2.63	0.00	3.31	0.03	29.42	0.59
BF5.1	1.16	0.03	0.08	0.06	0.08	0.00	0.00	0.10	87.79	0.05	10.61	0.00	0.04
BF5.2	52.99	2.74	1.20	8.89	1.37	0.85	0.00	2.39	2.05	3.08	1.03	0.85	22.56
BF5.4	1.29	0.05	0.10	0.07	0.07	1.19	0.18	0.13	0.03	0.10	0.20	0.02	96.58
BF5.5	12.46	0.28	0.28	0.65	3.81	5.76	6.32	0.98	3.16	0.37	0.70	0.14	65.09
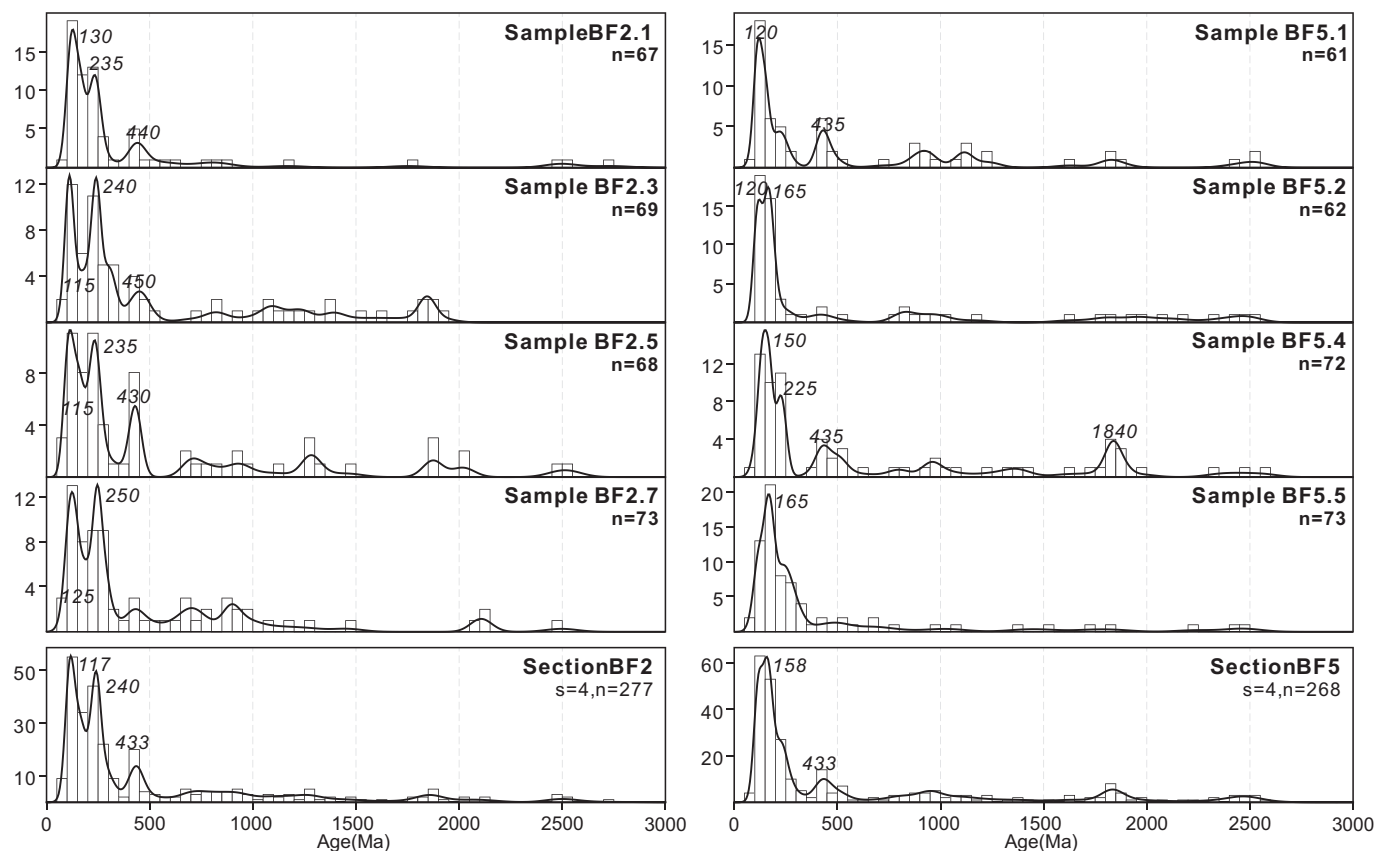
Fig. 8. Histograms and kernel density estimation (KDE) spectra for detrital zircon U-Pb ages of Baliojong sandstone samples from sections BF2 and BF5. s—number of samples; n—number of concordant analyses.

ages between the two sections is consistent with their different signatures of whole-rock geochemistry, heavy minerals, and zircon U-Pb ages (Figs. 6–8). Considering the potential Pb loss effect for youngest single grains and the conservative nature of age proxies based on multiple grains, we select the YGC2σ(3 +) proxy to represent the maximum depositional age, which is 86.8 Ma in section BF2 and 92.9 Ma in section BF5 (Fig. 9). Thus, the Baliojong turbidites were likely deposited around the Turonian–Coniacian, which is reasonably younger than the underlying Albian–Cenomanian cherts and Early Cretaceous basalts (Jasin and Tongkul, 2013; Wang et al., 2023).

3.4. Paleomagnetism of basalts and pelagic sediments

3.4.1. Sampling and methods

We collected core samples with a standard diameter of 25 mm for paleomagnetism using a petrol-powered drill from pillow basalts and cherts. A total of 147 pillow basalt samples (coded PB) was collected from sections B2, B3, and B4, and 48 samples were collected from red siltstones (coded PC) intercalated in the basal parts of the chert sequence in sections B2, B3, and B5 (Figs. 2 and 3C). The pillow basalt section of section B5 was of insufficient stratigraphic thickness to collect enough samples that would accurately sample paleosecular variation, while section B4 did not contain the rhythmic alternation of red siltstone and radiolarian chert. The orientation of the samples was measured in the field with a magnetic compass and inclinometer attached. Following sampling procedures for paleomagnetic poles recommended in Gerritsen et al. (2022), we collected a single core per basalt pillow or siltstone bed to optimize the chance of sampling individual spot read-

ings of the paleomagnetic field with each core. The pillow basalt sections were generally sufficiently thick to collect about 50 samples over at least 100 m of stratigraphy. Ten to twenty red siltstone samples were collected per section, from exposures of a few meters in thickness. Estimated bedding attitudes of pillow basalts are generally striking roughly N–S with a ~45° overturned dip. Our bedding estimates of the pillow basalts were like those measured in the directly overlying radiolarian cherts, although our estimation was somewhat steeper. As the bedding attitude of pillow basalts is difficult to measure, and as pillows may have a small primary dip, we will discuss how the use of the bedding attitudes of the radiolarian chert alters our results.

Paleomagnetic analyses were carried out at the paleomagnetic laboratory Fort Hoofddijk at Utrecht University, the Netherlands. The pillow basalt samples were subjected to stepwise alternating field (AF) demagnetization in a robotized setup (Mullender et al., 2016) and the red siltstone samples were subjected to stepwise thermal (TH) demagnetization. The magnetization of all samples was measured on a 2G DC-SQUID magnetometer. During this process, the samples were kept in a magnetically shielded room.

We used the online portal Paleomagnetism.org (Koymans et al., 2016; Koymans et al., 2020) for sample interpretation and statistical analysis. Demagnetization diagrams were plotted as orthogonal vector diagrams (Zijderveld, 1967) and magnetic components were determined using principal component analysis (Kirschvink, 1980). Components decaying towards the origin are not forced to the origin, except when demagnetization diagrams are noisy. We did not apply a maximum angular deviation cutoff, as it does not demonstrably influence the precision or position of a pole (Gerritsen et al., 2022), but the widely used cutoff of 15° would not have eliminated
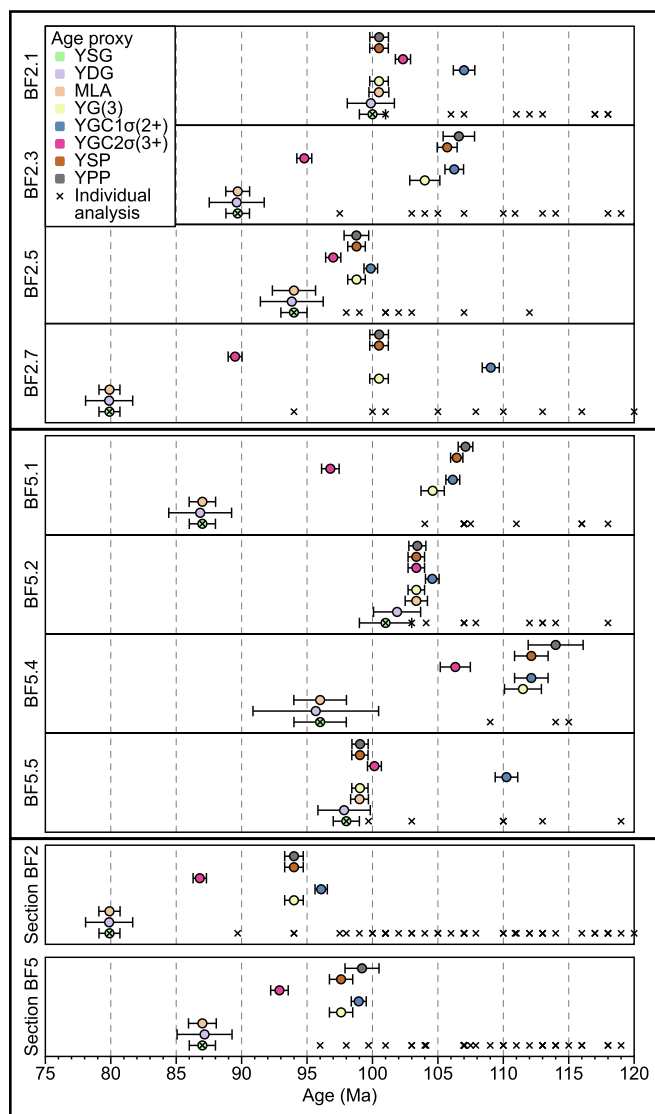
Fig. 9. Maximum depositional ages of Baliojong sandstone samples and grouped samples of sections BF2 and BF5, represented by a range of age proxies of detrital zircon U-Pb geochronology. Age proxies are calculated and visualized at 1σ and individual analyses of ≤ 120 Ma are also shown for comparison. YSG—the youngest single grain age; YDG—the age calculated by the 'Youngest Detrital Zircon' routine of Isoplot (Ludwig, 2003); MLA—the age calculated by ' Maximum Likelihood Age' algorithm of IsoplotR (Vermeesch, 2020); YG(3)—the weighted mean age of three youngest grains (Zhang et al., 2015); YGC1σ(2 +)—the weighted mean age of youngest cluster with two or more grains overlapping in age at 1σ (Dickinson and Gehrels, 2009); YGC2σ(3 +)—the weighted mean age of youngest cluster with three or more grains overlapping in age at 2σ (Dickinson and Gehrels, 2009); YSP—the weighted mean age of youngest cluster with a mean square weighted deviation (MSWD) of ~1 (Coutts et al., 2019); YPP—the youngest graphic peak age of kernel density estimation (KDE) spectrum.

data. Site mean directions were calculated using Fisher (1953) statistics on virtual geomagnetic poles following statistical procedures described in Deenen et al. (2011). To support the paleomagnetic results, thermomagnetic analysis was carried out with a modified horizontal translation Curie balance (Mullender et al., 1993) on selected samples to shed light on the dominant magnetic minerals. In the thermomagnetic analysis samples were stepwise heated to 700 °C in air with intermittent cooling segments to distinguish thermochemical alteration from magnetic behavior. The Curie temperature is estimated with the two-tangent method (Grommé et al., 1969). The temperature sequence is as follows for

the pillow basalts (in a cycling field between 200 and 300 mT): room temperature – 150 °C – 70 °C – 250 °C – 150 °C – 350 °C – 250 °C – 450 °C – 350 °C – 520 °C – 420 °C – 620 °C – 500 °C – 700 °C – room temperature. For the red silts it is (in a cycling field between 50 and 300 mT): room temperature – 250 °C – 150 °C – 350 °C – 250 °C – 450 °C – 350 °C – 520 °C – 420 °C – 620 °C – 500 °C – 700 °C – room temperature. To check for hematite behavior in a non-saturated applied field a second sample was stirred in the Curie balance sample holder after the 250 °C – room temperature partial run after which the complete stepwise thermomagnetic run was done (cf. De Boer and Dekkers, 1998).

3.4.2. Results and interpretation

In the thermomagnetic analysis, pillow basalts showed a gradual magnetization decay with minor removal of magnetic moment during the experiment, typical of maghemite that partly converts to less magnetic hematite (Fig. 10A). The Curie temperature is estimated at ~610 °C. Sample PB2.11 has this behavior to a greater extent than sample PB3.18 which reveals reversible magnetic behavior. This indicates that the maghemite (presumably thermally stabilized by some substituted Ti or Al) is probably formed in nature (i.e., not during the experiment itself). During the final cooling from 700 °C most maghemite converts to hematite as testified by the much lower final magnetization.

As expected, the red silts are much weaker (~10 to ~100 times) than the pillow basalts. The thermomagnetic behavior is dominated by hematite as indicated by the Néel temperature at 675 °C (Fig. 10B). Because high-coercivity hematite is not magnetically saturated in a field of 300 mT, the cooling segments are above the corresponding heating segments (Fig. 10B). This is an expression of acquisition of a magnetic moment and not of thermochemical alteration, as demonstrated by the stirring experiment in sample PC3.3. After the partial run to 250 °C, stirring of the sample when back at room temperature, the second run (again to 250 °C and then according to the full thermomagnetic experiment procedure) starts at approximately the same magnetic moment as at the beginning of the first run and not at the final magnetic moment of the first run. This indicates that the increase has a magnetic cause and is not induced by thermochemical alteration (De Boer and Dekkers, 1998). Rather surprisingly, magnetite – the carrier of the NRM signal – is below the limit of detection albeit that magnetite is formed during heating between 600 and 700 °C as manifested by marked increase in magnetic moment during cooling below 550 °C on the final cooling run. Sample PC3.3 shows this behavior to a larger extent than sample PC2.10 (Fig. 10B).

The NRM of the red silt samples shows a large secondary component up to ~200 °C (Fig. 10B). We speculate that this may be associated with the relatively large increase during the cooling segments in the thermomagnetic experiments after 250 and 350 °C, while the increase after cooling at higher temperatures up to 520 °C is barely noticeable (Fig. 10B). It would indicate a big proportion of very fine-grained hematite with low unblocking temperatures.

Samples from pillow basalts had initial NRM intensities ranging from 0.2 to 1.0 A/m, whereas the red silts had much lower intensities ranging from 200 to 2000 µA/m. Alternating field (AF) demagnetization in the pillow basalt (PB) samples generally shows a low coercivity component, followed by linear demagnetization trends towards the origin on the Zijderveld diagram (Fig. 11A). Maximum unblocking fields for the basalts mostly occur around 100 mT. In addition, at fields of 40–50 mT, a small component appears that deviates the trend away from the origin, which is interpreted as a laboratory-induced gyroremanent magnetization (GRM) (Dankers and Zijderveld, 1981). The datapoints influenced by GRM were not used to interpret the Characteristic Remanent Mag-
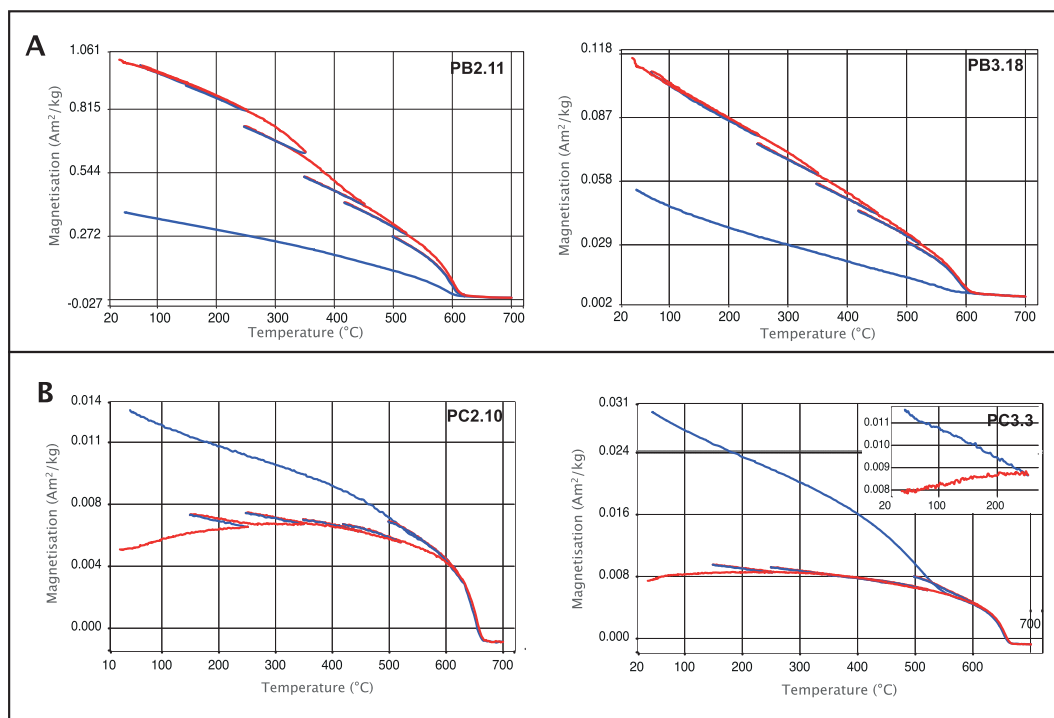
Fig. 10. Thermomagnetic curves measured on a modified horizontal tanslation Curie balance (Mullender et al., 1993). Heating segments in red, cooling in blue. Inset in PC3.3 shows the first heating cycle to 250 °C as part of the stirring experiment (see main text). (For interpretation of the references to colour in this figure legend, the reader is referred to the web version of this article.)

netization (ChRM). ChRM directions were interpreted based on a minimum of four consecutive data points.

The Zijderveld diagrams of the cherty siltstone samples (PC) are noisier than those of the basalts, but it is in most cases possible to discern a low-temperature component that is distinct from a high-temperature component that decays towards the origin (Fig. 12A). In the case of the pillow basalts, the high-coercivity component has northeasterly declinations (Fig. 11B), while in the case of the cherty siltstones, the high-temperature component has southerly declinations (Fig. 12B). We interpret these high-coercivity (PB sample set) or high-temperature (PC sample set) components as the ChRM directions. The ChRM directions of the pillow basalts were generally interpreted in the range of 30–50 mT. In some cases, the ChRM direction was already isolated from as low as 15 mT up to as high as 120 mT. ChRM directions of red siltstones were interpreted mostly in the range 250–510 °C, but could sometimes be interpreted up to 580 °C. It was possible to isolate a ChRM from most PB and PC samples, although a few samples were rejected due to erratic demagnetization behavior or strongly deviant paleomagnetic directions that we interpreted as the result of orientation errors or lightning strikes when a sample was almost completely demagnetized below 20 mT. Including these directions in the grand average would not have significantly shifted the computed paleomagnetic poles.

Mean paleomagnetic ChRM directions for all sites in geographic and tectonic (corrected for bedding tilt) coordinates are listed Table 4 and shown in Fig. 11B and 12B. All interpreted pillow basalt (PB) samples indicate the same polarity and the mean ChRM directions of the PB sites are different from the present-day GAD field in both geographic and tectonic coordinates (Fig. 11B). There is a slight variation in mean paleomagnetic direction between PB sites. In geographic coordinates, the directions of all three sections are significantly different (no Common True Mean Direction; CTMD; Tauxe et al., 2010) and vary by ~15° in declination and

inclination. In tectonic coordinates, the different PB sites also do not share a CTMD, but the variation in declination is smaller, up to maximum 8° (Table 4), while the inclination of PB2 is significantly steeper than for PB3 and PB4 (I = −26.9° ± 6.9° in PB2 versus I = −4.9° ± 7.2° in PB3 and 8.9° ± 7.1° for PB4). Fold tests per section are inconclusive (Tauxe and Watson, 1994; implemented in Paleomagnetism.org). When PB2 and PB3 are combined, the fold test is negative, but PB2 and PB4, as well as PB3 and PB4 yield an optimal clustering at ~90% unfolding (Fig. 11C). When all sites are combined, the fold test is inconclusive (Fig. 11C).

The red siltstone (PC) samples have an opposite polarity to the basalts (Fig. 12B). In geographic coordinates, the three sampled sections yield similar direction clusters, with average declinations varying from D = 163.8° ± 9.5° in PC2 to 173.1° ± 7.6° in PC3, although the inclinations vary more, from I = −0.2°±14.8° in PC2 to I = −29.4°±15.0° in PC5. This overall southeasterly direction cluster differs significantly from the ChRM directions in geographic coordinates from the pillow basalts, that when corrected for the opposite polarity, have a declination difference in geographic coordinates of ~40° (Fig. 11B and 12B; Table 4). This suggests that the ChRM directions of the red silts and the pillow lavas do not reflect the same paleomagnetic field, even though they are part of the same stratigraphic sequence, have similar bedding orientations, and are unlikely to be of significantly different age, since the red silts occur at the very base of the sedimentary sequence immediately overlying the pillow lavas. In tectonic coordinates, the magnetic directions of the cherts and pillows are also not antipodal (mean inclination of all PB and all PC sites is −14.4° and 5.9°, respectively, Table 4) and there is a rotation difference: mean declination of all PB and all PC sites is 319.0° and 159.2°, respectively. Between sites PC2 and 3 and the basaltic sections, this angle is approximately 20°. Locality PC5 has a bedding strike that is nearly 90° different from the other two PC sections because of local folding and thrusting. The mean paleomagnetic direction obtained
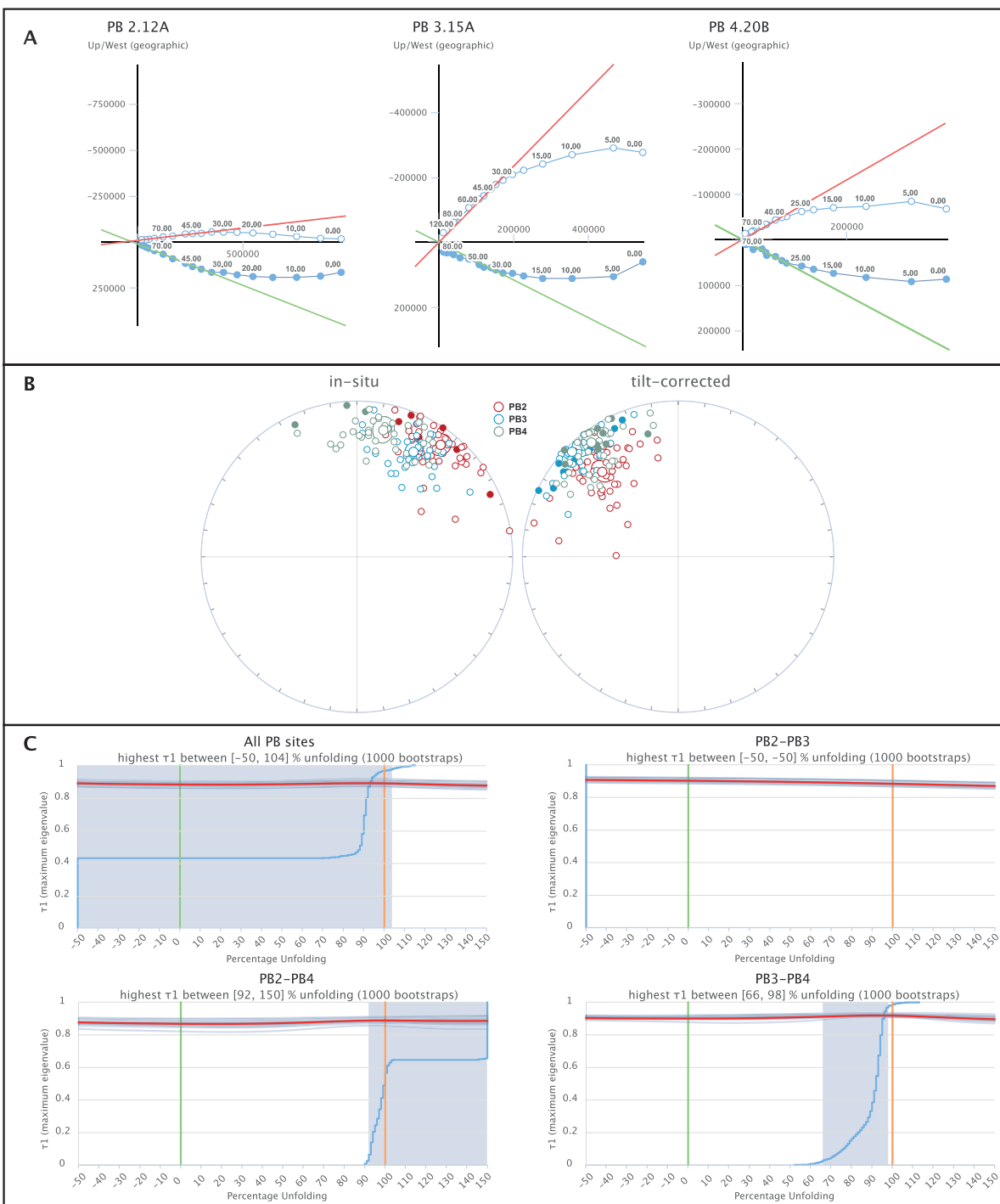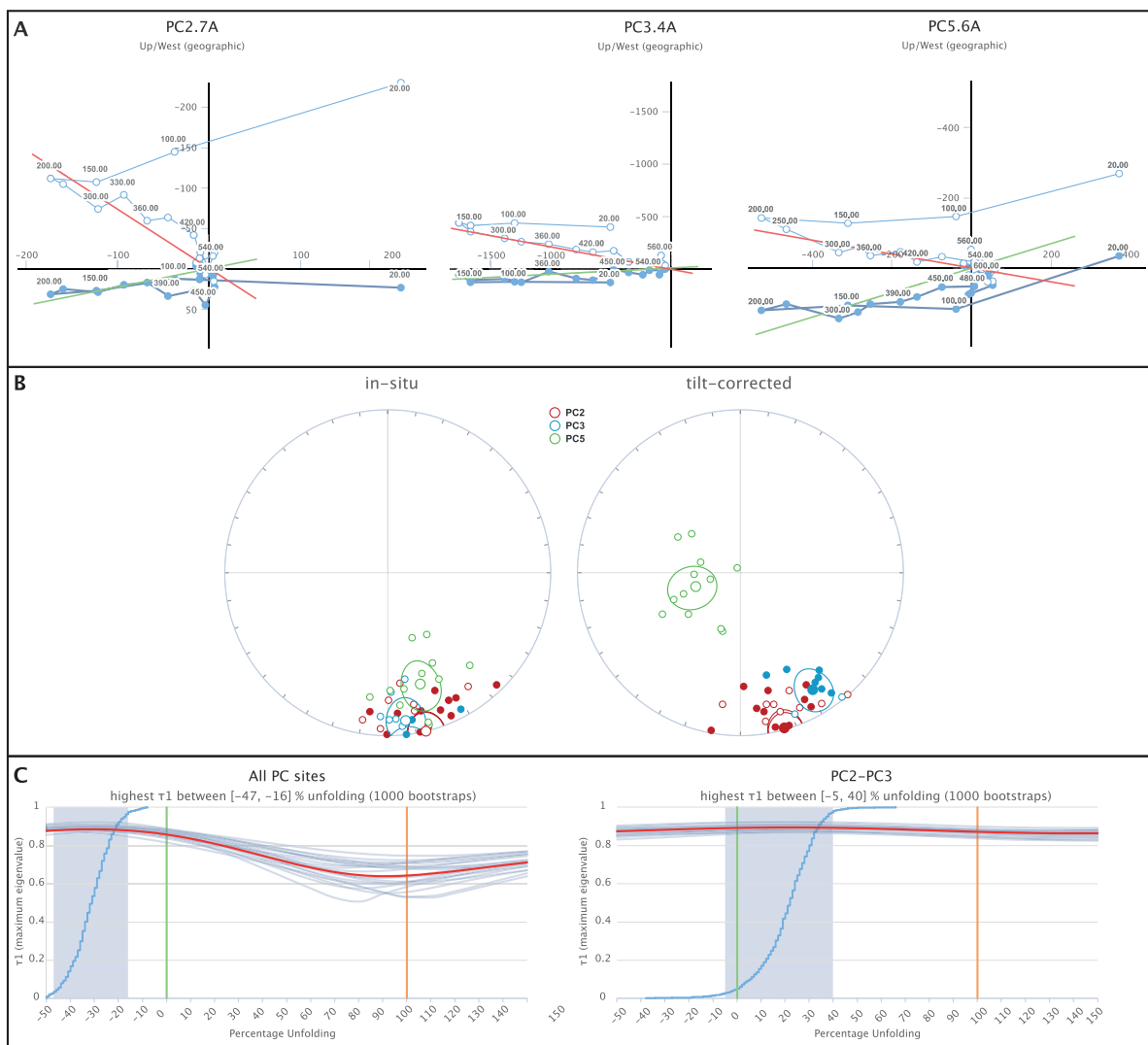
Fig. 11. Paleomagnetic results from PB sections. (A) Orthogonal vector diagrams of selected samples in geographic coordinates. Closed (open) symbols for declination (inclination); (B) Characteristic remanent magnetization (ChRM) directions, including means, per section in geographic (in-situ) and tectonic (tilt-corrected) coordinates; (C) Results of bootstrapped fold tests for different combinations of sections.

from PC5 is also very different to those of localities PC2 and PC3 that have a similar bedding orientation: PC2 and PC3 give in tectonic coordinates declinations/inclinations of 164.0°±6.2°/0.99°±12.40° (*N* = 20) and 148.2°±7.6°/16.5°±14.2° (*N* = 9), while PC5 has a declination of 252.40°±25.87° and inclination of −66.6°±12.3° (*N* = 12). The fold test of the red silt sections, in any combination, is either negative or inconclusive (Fig. 12C).

The magnetization of the pillow basalts in geographic coordinates is profoundly different from that of the remagnetized red siltstones, showing that they were magnetized at different times. In addition, the A95 values of the different PB localities all satisfy the criterion of Deenen et al. (2011, 2014), which suggests that the scatter that we obtained may be explained by paleosecular variation alone, and that paleosecular variation is adequately

Fig. 12. Paleomagnetic results from PC sections. (A) Orthogonal vector diagrams of selected samples in geographic coordinates. Closed (open) symbols for declination (inclination); (B) Characteristic remanent magnetization (ChRM) directions, including means, per section in geographic (in-situ) and tectonic (tilt-corrected) coordinates; (C) Results of bootstrapped fold tests for all PC sites and for PC2 and PC3.

represented in our sample set. Moreover, the fold test of the basalt sections of PB2 and PB3 gives optimal clustering at ~90% unfolding. We therefore interpret the magnetization of the pillow basalts as primary. Because pillow lavas do not form strictly horizontal bedding and topography may be somewhat rugged during deposition, we consider this as a positive fold test, whereby we note that this test shows that the uncertainty in the bedding tilt correction, and hence in the estimated inclination and paleolatitude, is larger than for normal sediments.

Based on the negative fold test of the PC samples, we interpret that the magnetic directions obtained from the red siltstone samples represent a remagnetization of these samples that occurred after folding (i.e., after the late Cretaceous accretion of the Baliojong OPS sequences), but before or during a phase of counterclockwise rotation given the declinations preserved in the sequence that differ significantly from the recent field. Paleomagnetic data from Cenozoic successions have revealed that Borneo underwent ~45° of counterclockwise rotation between the late Eocene and early Miocene (Fuller et al., 1999; Advokaat et al., 2018), during which time the Rajang-Crocker accretionary prism formed at the subduc-

tion zone that consumed the Proto-South China Sea below the Baliojong section (Hall et al., 2008). It seems plausible that the remagnetization occurred during this time period in a reverse magnetic field, possibly more or less halfway the rotation phase, i.e., sometime in the Oligocene, given the ~15° counterclockwise rotated overprint direction. Hence, we will not use the paleomagnetic results of the red siltstone samples for further tectonic interpretations.

We also tested what the effect on the interpreted inclination would be when the bedding attitude of the oldest overlying red beds would be used to estimate the bedding of the pillow basalts. In all sections, the inclination would become a few degrees shallower, suggesting a somewhat lower latitude. We thus consider the paleolatitudes that we computed using the in situ estimated bedding orientations of the pillows as maximum values.

Based on the interpretation that the pillow basalts carry a primary magnetic signal, we use the results in tectonic coordinates for our tectonic analysis. The declination data of the different sections suggest that they all underwent a similar rotation, of about 40° clockwise for a normal, southern hemisphere magnetization,

Table 4
Paleomagnetic results.

Section	Latitude (°)	Longitude (°)	N	Dec (°)	Inc (°)	k	a95	K	A95	A95$_{Min}$	A95$_{Max}$	ΔDx (°)	ΔIx (°)	λ (°)
In-situ (geographic) coordinates														
PB2	6.553785655	116.8883773	48	36.89	−11.09	19.93	4.73	27.91	3.96	2.55	7.16	3.98	7.71	−5.6
PB3	6.550319703	116.8836647	38	28.25	−24.26	27.72	4.49	35.87	3.93	2.80	8.29	4.03	6.87	−12.7
PB4	6.549018428	116.881319	42	11.78	−17.88	19.43	5.13	23.45	4.65	2.69	7.78	4.71	8.64	−9.16
PB all	6.551192463	116.8846622	128	26.22	−17.54	15.40	3.29	18.98	2.94	1.72	3.86	2.98	5.48	−8.98
PC2	6.55426563	116.8887535	20	166.40	−0.24	16.07	8.40	25.92	6.54	3.62	12.42	6.54	13.07	−0.12
PC3	6.55129203	116.8839535	9	173.06	−9.68	23.25	10.90	47.3	7.56	4.98	20.54	7.59	14.81	−4.87
PC5	6.546784599	116.8742342	12	163.77	−29.37	17.11	10.80	23.56	9.13	4.44	17.14	9.49	14.97	−15.71
PC all	6.551423357	116.8834503	41	167.23	−10.82	12.72	6.52	22.96	4.76	2.72	7.90	4.78	9.27	−5.46
Tilt-corrected (tectonic) coordinates														
Section	**Latitude (°)**	**Longitude (°)**	**N**	**Dec (°)**	**Inc (°)**	**k**	**a95**	**K**	**A95**	**A95$_{Min}$**	**A95$_{Max}$**	**ΔDx (°)**	**ΔIx (°)**	**λ (°)**
PB2	6.553785655	116.8883773	48	318.28	−27.68	19.93	4.73	23.23	4.36	2.55	7.16	4.51	7.31	−14.70
PB3	6.550319703	116.8836647	38	314.92	−4.90	27.72	4.49	42.23	3.62	2.80	8.29	3.62	7.19	−2.45
PB4	6.549018428	116.881319	42	322.76	−8.89	22.06	4.80	36.98	3.67	2.69	7.78	3.69	7.22	−4.47
PB all	6.551192463	116.8846622	128	318.75	−14.70	16.64	3.15	26.42	2.47	1.72	3.86	2.49	4.71	−7.47
PC2	6.55426563	116.8887535	20	163.98	0.99	16.07	8.40	28.53	6.22	3.62	12.42	6.22	12.43	0.49
PC3	6.55129203	116.8839535	9	148.17	16.53	23.25	10.90	47.18	7.57	4.98	20.54	7.66	14.23	8.44
PC5	6.546784599	116.8742342	12	252.43	−66.55	17.11	10.80	7.79	16.62	4.44	17.14	25.87	12.26	−49.05
PC all	6.551423357	116.8834503	41	168.77	−15.78	3.09	15.38	3.32	14.61	2.72	7.90	14.76	27.60	−8.04

or 140° counterclockwise for a reverse, northern hemisphere magnetization. The pillow basalts of a thrust slice below section 5 formed during the Early Cretaceous (c. 135 Ma; Wang et al., 2023), around which time the magnetic field underwent multiple polarity reversals, which means that the polarity of the magnetic field during magnetization is unknown. In addition, the Baliojong River section is a largely deformed accretionary prism, where large-scale rotations cannot be excluded. Hence, in our tectonic interpretation, we will discuss both the northern and southern hemisphere alternatives of formation of the pillow basalts. The inclination data suggest that the pillow basalts of section B2 formed at higher latitudes (14.7°±4.3°) than the pillow basalts of section B3 and B4 (2.5°±3.6° and 4.5°±3.7°, respectively), which may indicate that these sequences represent different tectonic nappes that accreted at a different time, whereby B2, with a significantly steeper inclination, may derive from a different nappe that accreted at a later time, because it is structurally deeper.

4. Discussion

Our data above suggest that the Baliojong OPS contains nappes that accreted in at least two events at the north Borneo margin. Based on maximum depositional ages of the foreland basin deposits, these events occurred around 92 Ma and 86 Ma, i.e., shortly before the end of Paleo-Pacific subduction inferred from the cessation of arc magmatism in the South China and Indochina regions, and the consequent trapping of the Proto-South China Sea lithosphere (Moss, 1998; Hall and Breitfeld, 2017; Advokaat and Van Hinsbergen, 2023). The interpretation that accretion occurred in at least two events is supported by the differences in geochemistry and heavy mineral composition between the two studies turbidite sections. Our data show that around 86–92 Ma, during the final stages of Paleo-Pacific subduction, an oceanic lithosphere with E-MORB geochemistry was subducting at the north Borneo margin that was then ∼45–50 Ma old (and currently 135 Ma; Wang et al., 2023). Finally, we show that the ocean floor formed at a paleolatitude ranging from ∼14° to ∼2°, although we cannot directly infer from the data whether these formed on the northern or southern hemisphere. Placing the reconstruction of Borneo of Advokaat and Van Hinsbergen (2023) in the paleomagnetic reference frame of Vaes et al. (2023) reveals that the latitude of accretion of the OPS sequences at 92–86 Ma was ∼3°N. This shows that the lithosphere that was underlying the Proto-South China Sea underwent a maximum net motion of up to 17° northwards or

11° southwards in the 45–50 Ma interval between its formation and its accretion in the Late Cretaceous. In the reconstruction of Zahirovic et al. (2014), accretion occurred at ∼4°S, which would indicate a smaller northward motion of 10° or a larger southward motion of 18°S. As the southward drift scenario does not straightforwardly explain active subduction below the South China margin, we consider the northward drift scenario more likely. We first use this information, combined with constraints from the accretionary prisms of the South China and Palawan margins to re-evaluate the plate kinematic history of the Proto-South China Sea and its motion relative to the Tethyan or Panthalassa plate systems. Next, we re-evaluate previously proposed causes of subduction cessation.

The lithosphere that was subducting below the SE China and Indochina margins prior to the late Cretaceous subduction cessation is typically loosely assigned to a Paleo-Pacific plate of the Panthalassa tectonic realm (e.g., Hall and Breitfeld, 2017; Zhang et al., 2019; Zheng et al., 2019). The simplest plate tectonic interpretation is then to infer that this lithosphere formed part of the Izanagi Plate (e.g., Zahirovic et al., 2014; Zhu et al., 2022), whose conjugate spreading records are preserved on the Pacific Plate (Nakanishi et al., 1992). We use our paleomagnetic data to test this hypothesis. To this end, we reconstructed the Proto-South China Sea oceanic crust as part of the Izanagi Plate from 85 Ma (the inferred end of its subduction), backwards in time to 135 Ma, whereby we connect the Panthalassa plate system to the Indo-Atlantic plate system using the reference frames of Torsvik et al. (2019) for the Panthalassa, and of Van der Meer et al. (2010) for the Indo-Atlantic frame prior to 85 Ma, which was shown to best reconcile paleomagnetic and plate kinematic constraints for the eastern Panthalassa-Caribbean realm by Boschman et al. (2019). We then place this connected plate system into the paleomagnetic reference frame of Vaes et al. (2023) to predict the paleolatitude of the Proto-South China Sea for a coordinate coinciding with our sampling locations, using the reconstruction of the Izanagi Plate of Boschman et al. (2021). This results in a predicted paleolatitude that is much farther south (∼30°S) than what is obtained from paleomagnetism in this study (Fig. 13). In other words, our data show that the oceanic crust that eventually floored the Proto-South China Sea embayment cannot have been part of the Izanagi Plate but must have been part of a plate with a slower northward motion component than the Izanagi Plate (Fig. 13). Although the paleolongitudinal motion of this plate is unknown, we may infer that it also has a westward motion component relative to Eurasia
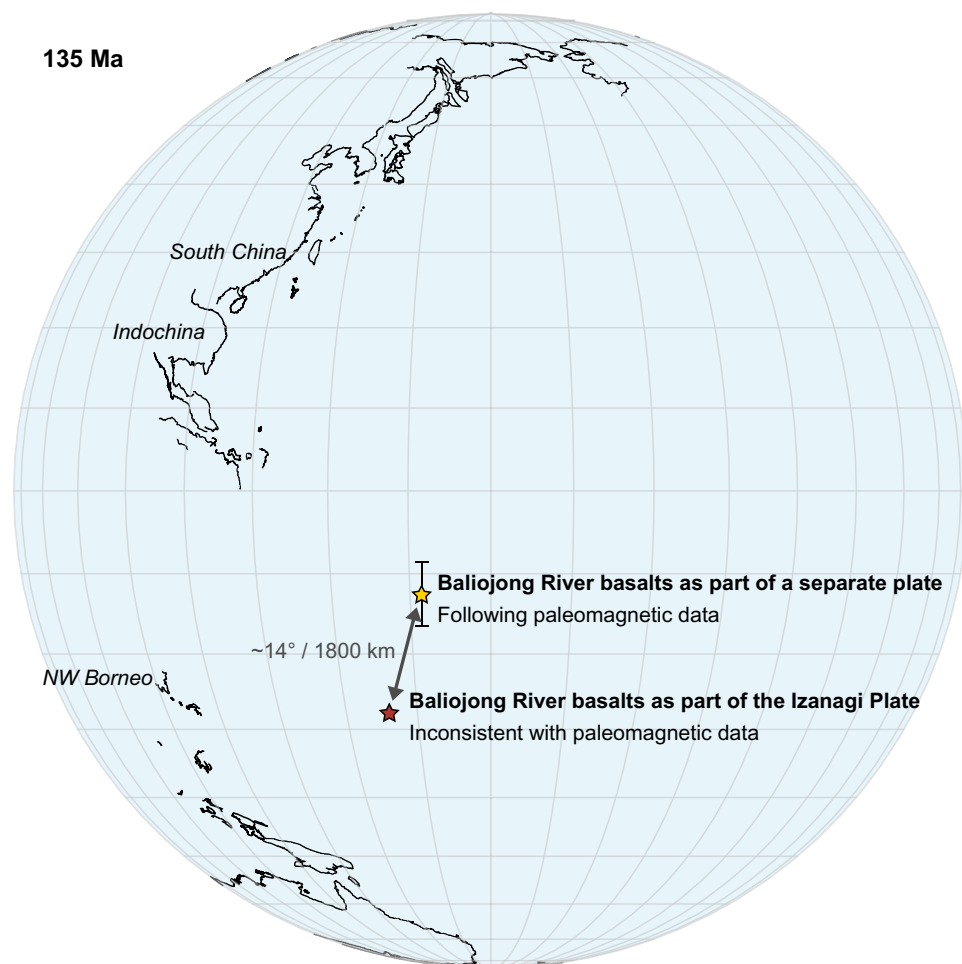
Fig. 13. Simplified tectonic reconstruction showing the reconstructed positions of the Baliojong River basalts as part of the Izanagi Plate and as part of a separate plate at 135 Ma. Reconstruction is made using the reconstructions of Advokaat and Van Hinsbergen (2023) and Boschman et al. (2021), in the paleomagnetic reference frame of Vaes et al. (2023). The uncertainty in the reference frame is ~1°, which is smaller than the star.

to satisfy the observation that there was subduction between South China, Indochina, as well as Borneo, whereby Borneo converged with South China (Advokaat and Van Hinsbergen, 2023).

Because the Izanagi Plate was moving northwestward at a higher rate than the Proto-South China Sea lithosphere, a subduction zone must have existed between these two plates, whereby Izanagi must have been in a downgoing plate position. A magmatic arc may thus have formed on the eastern boundary of the Proto-South China Sea lithosphere. We infer that the island arc volcanics of c. 100 Ma found in the Cenozoic accretionary prisms of from West Luzon and South Palawan (Pasco et al., 2019; Dycoco et al., 2021), which formed when the Proto-South China Sea eventually subducted, are remains of this intra-oceanic island arc. Interestingly, Van der Meer et al. (2012) inferred such a scenario from lower mantle tomographic images, from which they inferred that in Jurassic to Early Cretaceous time, the Panthalassa plates that surrounded the Pacific plate must have been subducting below an oceanic plate system to the west that was itself separated from the Neotethyan realm by subduction zones. They termed this plate system the 'Pontus Ocean' and named the intervening plate boundary the Telkhinia subduction zone. The relics of 100 Ma arc volcanoes found in the Palawan and west Luzon accretionary prisms may then be fragments of the Telkhinia arc. Because the tomographic resolution shallower than ~2000 km depth was too low for a meaningful interpretation, Van der Meer et al. (2012) were not able to reconstruct when and how the Telkhinia subduction

zone came to an end. We infer that this plate boundary eventually evolved to the Philippines-Proto-South China Sea boundary, although detailed kinematic restoration is needed to systematically reconstruct its kinematic history. We infer, however, that the Proto-South China Sea lithosphere was the last remains of the Pontus Ocean and refer to it as the Pontus Plate. The existence of a plate such as the Pontus Plate was previously suggested by Seton et al. (2012), who postulated that a 'Junction Plate' separated from the Panthalassa plates existed between 140 Ma and 70 Ma to account for convergence.

We now evaluate why the Pontus Plate did not entirely subduct in the late Cretaceous, but first came to an cessation around 85 Ma, after which it finally subducted between ~40 Ma and 15 Ma. There are several models that explain the end of subduction in the circum-Proto-South China Sea region. One model that explains the end of magmatism in SE China and Indochina infers that subduction continued beyond 85 Ma, but retreated southward, which resulted in the opening of the Proto-South China Sea as a back-arc basin analogous to e.g., the Sea of Japan (e.g., He and Xu, 2012; Li et al., 2012; Li et al., 2014; Zahirovic et al., 2014; Yan et al., 2017). The model, however, does not explain the presence of a subduction record that ceased at the Borneo margin. Moreover, the ~100 Ma basalts accreted in Palawan during the Oligocene (Dycoco et al., 2021) show that the crust of the Proto-South China Sea formed before the end of South China arc magmatism: the Proto-South China Sea crust can therefore not have formed in a

post-85 Ma back-arc basin. Finally, a back-arc basin scenario does not explain how an accretionary prism with Jurassic seamounts was preserved to the north of the Proto-South China Sea in the South China margin (Xu et al., 2022). We conclude that the back-arc basin model does not satisfy the geological data from the accreted OPS sequences in the South China, Palawan, and North Borneo margins.

Subduction thus ceased during the Late Cretaceous, even though oceanic crust remained in the foreland. Such an cessation of oceanic subduction may conceptually be explained by the arrival of a mid-oceanic ridge in the subduction zone, as occurred at the

continental margin of Antarctica in the south Pacific (Eagles, 2004; Van de Lagemaat et al., 2023), and in the eastern Pacific adjacent to California and Baja California (Atwater, 1989). However, a ridge arrival-scenario is readily excluded for the Proto-South China Sea, because the last subducted oceanic crust that left an accretionary record was at least ∼40 Ma old in the Baliojong OPS (this study), and ∼60 Ma old in the South China margin (Xu et al., 2022).

We therefore propose that subduction ceased because the resistance against subduction of the oceanic lithosphere increased, likely because of enhanced buoyancy. Such a scenario has been
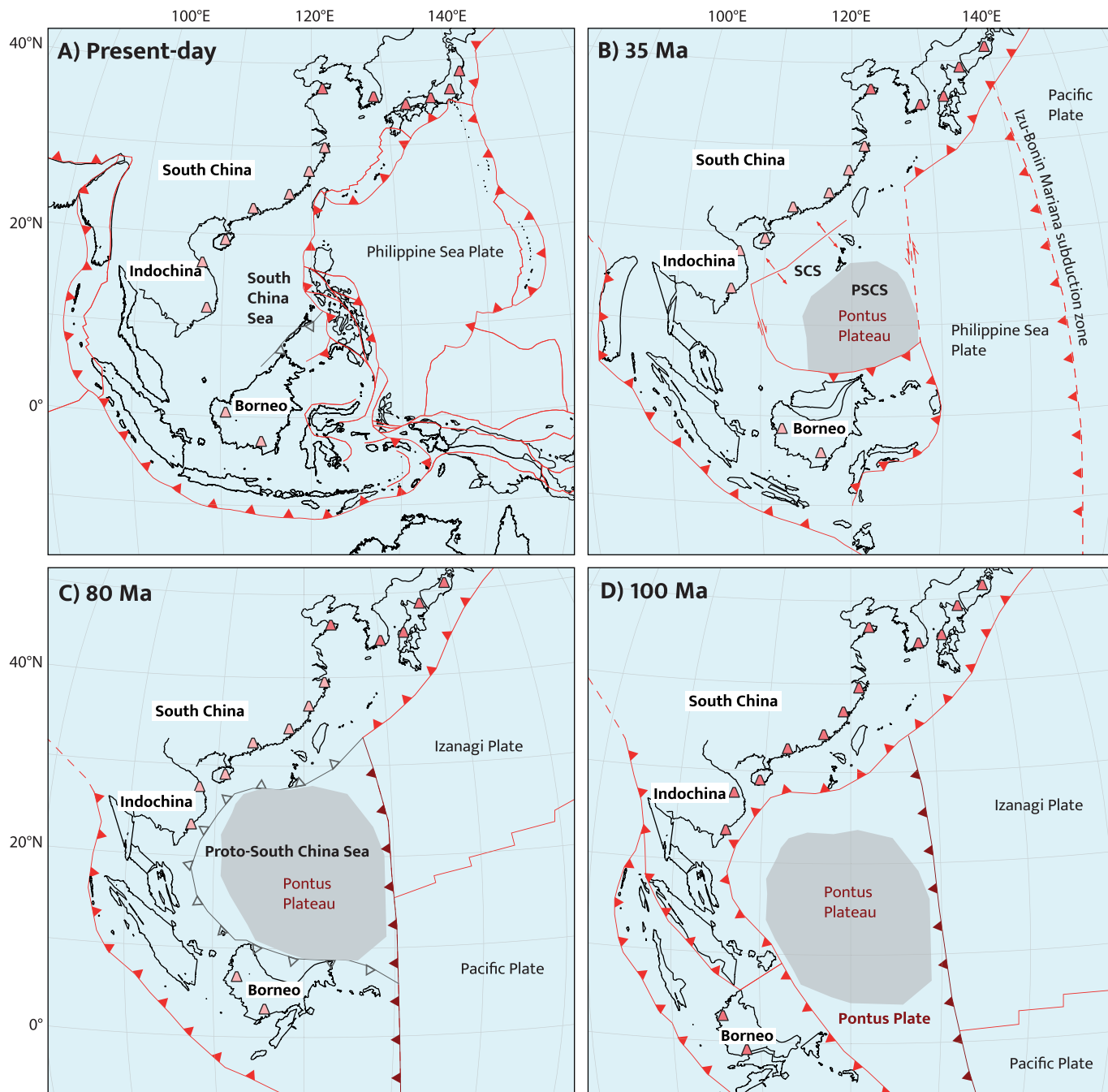
Fig. 14. Simplified Late Mesozoic - Cenozoic tectonic evolution of the NW Panthalassa region, including the Pontus Plate and the Pontus-Izanagi subduction zone, in a South China-fixed reference frame. Reconstruction of SE Asia based on Advokaat and Van Hinsbergen (2023). Dark pink cones indicate active arc magmatism, light pink cones indicate extinct arc magmatism. Active plate boundaries in red, former plate boundaries in gray. New tectonic features based on this study in dark red. (For interpretation of the references to colour in this figure legend, the reader is referred to the web version of this article.)

proposed before to explain the cessation of subduction below the SE China margin. Hall (2012) and Niu et al. (2015) speculated that subduction may have ceased by the arrival of a microcontinent. While such a scenario may explain subduction cessation, there is no geological evidence for the arrival of a microcontinent in the Cretaceous or its consumption during Eocene-early Miocene subduction below Borneo and Palawan – on the contrary, all accreted records consist of OPS sequences that show no evidence that continental crust was involved in the subduction around the time of subduction cessation.

Xu et al. (2022) proposed that the arrival of an oceanic plateau led to the cessation of subduction, and this is a promising explanation. They based their interpretation on the discovery of two Lower Cretaceous seamounts in the south China margin west of Taiwan region (China). The geochemical signatures that we obtained from the pillow basalts of the Baliojong OPS sequence give an E-MORB geochemistry (Fig. 4). According to Xia and Li (2019), oceanic plateau basalts generally have a Transitional-MORB (T-MORB) to E-MORB geochemistry. Samples from the Ontong Java and Caroline plateaus in the West Pacific, for example, display T-MORB to E-MORB geochemical affinities (Zhang et al., 2020). Our results may thus indicate that thickened oceanic lithosphere also arrived at the north Borneo margin shortly before the ∼85 Ma of subduction cessation. Interestingly, however, very different ages were obtained from the magmatic rocks that accreted at the Paleo-Pacific margins of South China and SE Asia: ∼154 Ma in the north, at the SE China continental margin (Xu et al., 2022), ∼135 Ma in NW Borneo (Wang et al., 2023), whereas ∼100 Ma arc volcanoes remained in the eastern Proto-South China Sea that eventually ended up in the Palawan and west Luzon accretionary prisms (Pasco et al., 2019; Dycoco et al., 2021).

The different ages of accreted mafic rocks suggest that it was perhaps not a single Large Igneous Province like the Ontong-Java Plateau that arrived in the trench, as those generally form within a few million years. Instead, the Proto-South China Sea embayment may have been underlain by a composite plateau that was thickened by multiple magmatic events. In the east, this included the 'Telkhinia' arc. Elsewhere, such thickened oceanic crust may have formed in a tectonic setting analogous to the "hotspot-highway" in the Pacific (Jackson et al., 2010) that comprises multiple seamount chains that formed from different hotspot sources in relative proximity, forming a region of thickened oceanic crust with different ages. Alternatively, the different ages may be related to a main event of oceanic plateau formation in the latest Jurassic, with secondary volcanism after the main stage of plateau formation. The Ontong Java Plateau, for example, had a main stage of formation at around 117–118 Ma, but later-stage magmatism also occurred from ∼111–108 Ma and at c. 90 Ma (Mahoney et al., 1993; Fitton et al., 2004; Korenaga, 2005; Davidson et al., 2023). The c. 20 Ma age difference in the Pontus Plate volcanoes is therefore not unusual. Regardless of whether it was a true Large Igneous Province or a 'hotspot-highway', we suggest that end of subduction at the continental margin surrounding the Pontus Plate in the Proto-South China Sea embayment may have been related to the arrival of thickened oceanic crust, the hypothetical Pontus Plateau (Fig. 14).

Even though we infer that thickened crust initially blocked a major and long-lived subduction zone, this fragment of oceanic lithosphere was eventually lost to subduction during the Cenozoic, which suggests that such crust is subductable after all – which must be the case since records of ancient intra-oceanic plateaus are rare (Van Hinsbergen and Schouten, 2021). A similar history has been reconstructed from the Hikurangi Plateau in the SW Pacific. The Hikurangi Plateau is a fragment of the Ontong-Java-Nui Large Igneous Province (Taylor, 2006; Chandler et al., 2012), and its arrival in the New Zealand trench is thought to have caused the shutdown of local subduction at the East Gondwana subduction zone in the Late Cretaceous (e.g., Billen and Stock, 2000; Davy et al., 2008; Van de Lagemaat et al., 2023). Nonetheless, that same plateau is subducting today at the Hikurangi Trench (Collot and Davy, 1998; Timm et al., 2014; Hoernle et al., 2021). It was probably able to stop subduction in the Late Cretaceous because it formed part of a relatively small plate (the Hikurangi Plate; Van de Lagemaat et al., 2023). Today, it forms part of the major Pacific Plate, whose westward motion is forcing the Hikurangi Plate below the Australian Plate at the North Island of New Zealand.

Like the Hikurangi Plate, the Pontus Plate was by the Late Cretaceous reduced to a relatively small surface area (Fig. 14). Moreover, it was surrounded by subduction zones. This suggests that the obstruction of the subduction caused by the arrival of an oceanic plateau on the Pontus Plate is geodynamically straightforward. Relative convergence at its eastern boundary that was already being accommodated simply increased to accommodate all Izanagi-Eurasia convergence after the Pontus Plate itself stopped subducting. Subsequently, in the Eocene, when it formed part of the much larger Eurasian Plate, it was ultimately forced to subduct below NW Borneo and the Cagayan arc, likely induced by the 45 Ma pulse of northward motion of the Australian Plate, that triggered a northward motion and counterclockwise rotation of Borneo (Advokaat et al., 2018). And when the Pontus Plate/Proto-South China Sea eventually subducted, it forced the opening of the South China Sea in its wake, in a downgoing plate position. We speculate that eclogitization of the thickened oceanic crust may have generated a slab pull that was so strong that it broke the former accretionary prism at the South China margin to form the South China Sea basin.

5. Conclusions

In this paper, we investigated the potential geodynamic causes of enigmatic subduction cessation along the South China Sea margin, which led to the formation of the Proto-South China Sea that from Late Cretaceous to Eocene time intervened Borneo and South China, after which it subducted in the Oligocene-early Miocene. To this end, we studied the youngest accreted rocks that formed at the North Borneo margin during the latest stages of subduction of the Proto-South China Sea lithosphere below northern Borneo, just prior to late Cretaceous subduction cessation. This record is preserved as well-exposed, deformed Ocean Plate Stratigraphy (OPS) remains of the Baliojong River section in Sabah, NW Borneo. We report a detailed analysis of this OPS section. Based on our results from pillow basalt geochemistry, radiolarian biostratigraphy, and detrital zircon geochemistry, geochronology, and provenance, and paleomagnetism we conclude the following:

(1) The Baliojong River exposes different thrust slices of OPS that were likely accreted in at least two events, inferred from the slight variation in basalt geochemistry, sediment provenance and maximum depositional ages, and the different paleolatitudes.
(2) These thrust slices of oceanic crust accreted at different times in the Late Cretaceous, during the final stages of subduction in the Proto-South China Sea embayment, at c. 92 Ma and 86 Ma.
(3) The oceanic crust formed at near-equatorial latitudes around 135 Ma. This low latitude excludes that the lithosphere was part of the Izanagi Plate whose spreading history is reconstructed from Pacific Plate anomalies. Instead, the Proto-South China Sea lithosphere was part of a slower NW moving plate below which Izanagi subducted. Remnants of this

subduction zone are identified in accretionary prisms on Palawan and western Luzon as ~100 Ma arc volcanic remains. Such a plate system was previously inferred from lower mantle slab remnants (Van der Meer et al., 2012), and following that work, we name the plate to which the Proto-South China Sea lithosphere belonged the Pontus Plate, and the arc remains on its eastern margin the Telkhinia Arc.

(4) Our geochemical data are consistent with formation of the Baliojong basalts as part of an oceanic plateau. Combined with previously published evidence for seamount accretion in the Late Cretaceous at the South China Sea margin and the Telkhinia arc remains, we infer that subduction cessation resulted from obstruction of the trench induced by thickened, buoyant oceanic lithosphere (the 'Pontus Plateau'), which may have been comparable to the Ontong Java plateau or, alternatively, a series of seamount chains such as the Hotspot Highway of the Central Pacific. Its arrival at the trench caused the end of subduction in the Proto-South China Sea embayment in the Late Cretaceous.

(5) Final subduction of the Proto-South China Sea lithosphere and the conceptual Pontus Plateau below the Borneo and Palawan margins resulted from convergence between Borneo and South China that was likely induced by an Australia-Eurasia convergence pulse. We speculate that the opening of the South China Sea in the downgoing plate in the wake of the subducting Proto-South China Sea may have resulted from enhanced slab pull when the thickened subducting crust underwent eclogitization.

CRediT authorship contribution statement

Suzanna H.A. van de Lagemaat: Formal analysis, Investigation, Data curation, Writing – original draft, Visualization. **Licheng Cao:** Formal analysis, Investigation, Data curation, Writing – review & editing, Visualization. **Junaidi Asis:** Formal analysis, Investigation, Data curation, Writing – review & editing. **Eldert L. Advokaat:** Formal analysis, Investigation, Data curation, Writing – review & editing. **Paul R.D. Mason:** Formal analysis, Data curation, Writing – review & editing. **Mark J. Dekkers:** Formal analysis, Data curation, Writing – review & editing. **Douwe J.J. van Hinsbergen:** Formal analysis, Investigation, Data curation, Writing – review & editing, Supervision, Funding acquisition.

Declaration of Competing Interest

The authors declare that they have no known competing financial interests or personal relationships that could have appeared to influence the work reported in this paper.

Acknowledgements

Data statement

Geochemical data of the pillow basalts and geochemical and heavy mineral data of the sandstones is provided as data tables in the main text. Zircon U-Pb data table is provided as Supplementary Data Table S2. Paleomagnetic data will be made available in the Paleomagnetism.org database (Koymans et al., 2016, 2020), and the MagIC database (Jarboe et al., 2012).

Appendix A. Supplementary data

Supplementary data to this article can be found online at https://doi.org/10.1016/j.gsf.2023.101752.

References

Advokaat, E.L., Marshall, N.T., Li, S., Spakman, W., Krijgsman, W., van Hinsbergen, D.J., 2018. Cenozoic rotation history of Borneo and Sundaland, SE Asia revealed by paleomagnetism, seismic tomography, and kinematic reconstruction. Tectonics 37 (8), 2486–2512.

Advokaat, E.L., van Hinsbergen, D.J.J., 2023. Finding Argoland: Reconstructing a microcontinental archipelago from the SE Asian accretionary orogen. Gondwana Res. in Press.. https://doi.org/10.1016/j.gr.2023.10.005.

Atwater, T.M., 1989. Plate tectonic history of the northeast Pacific and western North America. In: Winterer, E.L., Hussong, D.M., Decker, R.W. (Eds.), The Eastern Pacific Ocean and Hawaii. Geological Society of America, The Geology of North America, pp. 21–72.

Aurelio, M.A., Forbes, M.T., Taguibao, K.J.L., Savella, R.B., Bacud, J.A., Franke, D., Pubellier, M., Savva, D., Meresse, F., Steuer, S., Carranza, C.D., 2014. Middle to Late Cenozoic tectonic events in south and central Palawan (Philippines) and their implications to the evolution of the south-eastern margin of South China Sea: Evidence from onshore structural and offshore seismic data. Mar. Pet. Geol. 58, 658–673.

Barckhausen, U., Engels, M., Franke, D., Ladage, S., Pubellier, M., 2014. Evolution of the South China Sea: Revised ages for breakup and seafloor spreading. Mar. Pet. Geol. 58, 599–611.

Batara, B., Xu, C., 2022. Evolved magmatic arcs of South Borneo: Insights into Cretaceous slab subduction. Gondwana Res. 111, 142–164.

Berry, K., 2022. A Classopollis, "spike" in the Rugubivesiculites Zone of the Kayan Sandstone, western Sarawak, Borneo, suggests a Danian age for these deposits. Rev. Palaeobotany Palynol. 304, 104728.

Billen, M.I., Stock, J., 2000. Morphology and origin of the Osbourn Trough. J. Geophys. Res.: Solid Earth 105 (B6), 13481–13489.

Boschman, L.M., Van der Wiel, E., Flores, K.E., Langereis, C.G., Van Hinsbergen, D.J.J., 2019. The Caribbean and Farallon plates connected: Constraints from stratigraphy and paleomagnetism of the Nicoya Peninsula, Costa Rica. J. Geophys. Res.: Solid Earth 124 (7), 6243–6266.

Boschman, L.M., Van Hinsbergen, D.J.J., Langereis, C.G., Flores, K.E., Kamp, P.J.J., Kimbrough, D.L., Ueda, H., Van de Lagemaat, S.H.A., Van der Wiel, E., Spakman, W., 2021. Reconstructing lost plates of the Panthalassa Ocean through paleomagnetic data from circum-Pacific accretionary orogens. Am. J. Sci. 321 (6), 907–954.

Breitfeld, H.T., Hall, R., Galin, T., Forster, M.A., BouDagher-Fadel, M.K., 2017. A Triassic to Cretaceous Sundaland-Pacific subduction margin in West Sarawak, Borneo. Tectonophysics 694, 35–56.

Breitfeld, H.T., Hall, R., Galin, T., BouDagher-Fadel, M.K., 2018. Unravelling the stratigraphy and sedimentation history of the uppermost Cretaceous to Eocene sediments of the Kuching Zone in West Sarawak (Malaysia), Borneo. J. Asian Earth Sci. 160, 200–223.

Breitfeld, H.T., Davies, L., Hall, R., Armstrong, R., Forster, M., Lister, G., Thirlwall, M., Grassineau, N., Hennig-Breitfeld, J., van Hattum, M.W., 2020. Mesozoic Paleo-Pacific subduction beneath SW Borneo: U-Pb geochronology of the Schwaner granitoids and the Pinoh metamorphic group. Front. Earth Sci. 8, 568715.

Briais, A., Patriat, P., Tapponnier, P., 1993. Updated interpretation of magnetic anomalies and seafloor spreading stages in the South China Sea: Implications for the Tertiary tectonics of Southeast Asia. J. Geophys. Res.: Solid Earth 98 (B4), 6299–6328.

Burton-Johnson, A., Macpherson, C.G., Millar, I.L., Whitehouse, M.J., Ottley, C.J., Nowell, G.M., 2020. A Triassic to Jurassic arc in north Borneo: Geochronology, geochemistry, and genesis of the Segama Valley Felsic Intrusions and the Sabah ophiolite. Gondwana Res. 84, 229–244.

Cao, X., Flament, N., Li, S., Müller, R.D., 2021b. Spatio-temporal evolution and dynamic origin of Jurassic-Cretaceous magmatism in the South China Block. Earth-Sci. Rev. 217, 103605.

Cao, L., Shao, L., Qiao, P., Cui, Y., Zhang, G., Zhang, X., 2021a. Formation and paleogeographic evolution of the Palawan continental terrane along the Southeast Asian margin revealed by detrital fingerprints. GSA Bull. 133 (5–6), 1167–1193.

Cawood, P.A., Hawkesworth, C.J., Dhuime, B., 2012. Detrital zircon record and tectonic setting. Geology 40, 875–878.

Chandler, M.T., Wessel, P., Taylor, B., Seton, M., Kim, S.S., Hyeong, K., 2012. Reconstructing Ontong Java Nui: Implications for Pacific absolute plate motion, hotspot drift and true polar wander. Earth Planet. Sci. Lett. 331, 140–151.

Collot, J.Y., Davy, B., 1998. Forearc structures and tectonic regimes at the oblique subduction zone between the Hikurangi Plateau and the southern Kermadec margin. J. Geophys. Res.: Solid Earth 103 (B1), 623–650.

Conand, C., Mouthereau, F., Ganne, J., Lin, A.T.S., Lahfid, A., Daudet, M., Mesalles, L., Giletycz, S., Bonzani, M., 2020. Strain partitioning and exhumation in oblique Taiwan collision: Role of rift architecture and plate kinematics. Tectonics 39 (4), e2019TC005798.

Coutts, D.S., Matthews, W.A., Hubbard, S.M., 2019. Assessment of widely used methods to derive depositional ages from detrital zircon populations. Geosci. Front. 10, 1421–1435.

Dankers, P.H.M., Zijderveld, J.D.A., 1981. Alternating field demagnetization of rocks, and the problem of gyromagnetic remanence. Earth Planet. Sci. Lett. 53 (1), 89–92.

Davidson, P.C., Koppers, A.A., Sano, T., Hanyu, T., 2023. A younger and protracted emplacement of the Ontong Java Plateau. Science 380 (6650), 1185–1188.

Davies, L., Hall, R., Armstrong, R., 2014. Cretaceous crust in SW Borneo: petrological, geochemical and geochronological constraints from the Schwaner Mountains. Proceedings, Indonesian Petroleum Association, Thirty-Eighth Annual Convention & Exhibition.

Davy, B., Hoernle, K., Werner, R., 2008. Hikurangi Plateau: Crustal structure, rifted formation, and Gondwana subduction history. Geochem. Geophys. Geosyst. 9 (7), Q07004.

De Boer, C.B., Dekkers, M.J., 1998. Thermomagnetic behaviour of haematite and goethite as a function of grain size in various non-saturating magnetic fields. Geophys. J. Int. 133 (3), 541–552.

Deenen, M.H., Langereis, C.G., van Hinsbergen, D.J., Biggin, A.J., 2011. Geomagnetic secular variation and the statistics of palaeomagnetic directions. Geophys. J. Int. 186 (2), 509–520.

Deenen, M.H., Langereis, C.G., van Hinsbergen, D.J., Biggin, A.J., 2014. Erratum: Geomagnetic secular variation and the statistics of palaeomagnetic directions. Geophys. J. Int. 197 (1), 643.

Dickinson, W.R., Gehrels, G.E., 2009. Use of U-Pb ages of detrital zircons to infer maximum depositional ages of strata: A test against a Colorado Plateau Mesozoic database. Earth Planet Sci. Lett. 288, 115–125.

Dycoco, J.M.A., Payot, B.D., Valera, G.T.V., Labis, F.A.C., Pasco, J.A., Perez, A.D., Tani, K., 2021. Juxtaposition of Cenozoic and Mesozoic ophiolites in Palawan island, Philippines: New insights on the evolution of the Proto-South China Sea. Tectonophysics 819, 229085.

Eagles, G., 2004. Tectonic evolution of the Antarctic-Phoenix plate system since 15 Ma. Earth Planet. Sci. Lett. 217 (1–2), 97–109.

Faure, M., Ishida, K., 1990. The Mid-Upper Jurassic olistostrome of the west Philippines: a distinctive key-marker for the North Palawan block. J. Southeast. Asian Earth Sci. 4 (1), 61–67.

Fisher, R.A., 1953. Dispersion on a sphere. Proc. Royal Soc. Lond. Ser. A. Math. Phys. Sci. 217 (1130), 295–305.

Fitton, J.G., Mahoney, J.J., Wallace, P.J., Saunders, A.D., 2004. Origin and evolution of the Ontong Java Plateau: introduction. Geol. Soc. London Spec. Pub. 229 (1), 1–8.

Floyd, P.A., Leveridge, B.E., 1987. Tectonic environment of the Devonian Gramscatho basin, south Cornwall: framework mode and geochemical evidence from turbiditic sandstones. J. Geol. Soc. 144, 531–542.

Fuller, M., Ali, J.R., Moss, S.J., Frost, G.M., Richter, B., Mahfi, A., 1999. Paleomagnetism of borneo. J. Asian Earth Sci. 17 (1–2), 3–24.

Gerritsen, D., Vaes, B., van Hinsbergen, D.J.J., 2022. Influence of data filters on the position and precision of paleomagnetic poles: what is the optimal sampling strategy?. Geochem. Geophys. Geosyst. 23 (4), e2021GC010269.

Gibaga, C.R.L., Arcilla, C.A., Hoang, N., 2020. Volcanic rocks from the Central and Southern Palawan Ophiolites, Philippines: tectonic and mantle heterogeneity constraints. J. Asian Earth Sci. X, 4, 100038.

Gradstein, F.M., Ogg, J.G., Schmitz, M.D., Ogg, G.M., 2020. Geologic Time Scale 2020. Elsevier. https://doi.org/10.1016/C2020-1-02369-3.

Grommé, C.S., Wright, T.L., Peck, D.L., 1969. Magnetic properties and oxidation of iron-titanium oxide minerals in Alae and Makaopuhi lava lakes, Hawaii. J. Geophys. Res. 74 (22), 5277–5293.

Hall, R., 2002. Cenozoic geological and plate tectonic evolution of SE Asia and the SW Pacific: computer-based reconstructions, model and animations. J. Asian Earth Sci. 20 (4), 353–431.

Hall, R., 2012. Late Jurassic-Cenozoic reconstructions of the Indonesian region and the Indian Ocean. Tectonophysics 570, 1–41.

Hall, R., Breitfeld, H.T., 2017. Nature and demise of the Proto-South China Sea. Bull. Geol. Soc. Malaysia 63, 61–67.

Hall, R., van Hattum, M.W., Spakman, W., 2008. Impact of India-Asia collision on SE Asia: the record in Borneo. Tectonophysics 451 (1–4), 366–389.

He, Z.Y., Xu, X.S., 2012. Petrogenesis of the Late Yanshanian mantle-derived intrusions in southeastern China: response to the geodynamics of Paleo-Pacific plate subduction. Chem. Geol. 328, 208–221.

Hennig, J., Breitfeld, H.T., Hall, R., Nugraha, A.S., 2017. The Mesozoic tectono-magmatic evolution at the Paleo-Pacific subduction zone in West Borneo. Gondwana Res. 48, 292–310.

Hennig-Breitfeld, J., Breitfeld, H.T., Sang, D.Q., Vinh, M.K., Van Long, T., Thirlwall, M., Cuong, T.X., 2021. Ages and character of igneous rocks of the Da Lat Zone in SE Vietnam and adjacent offshore regions (Cuu Long and Nam Con Son basins). J. Asian Earth Sci. 218, 104878.

Hieu, P.T., Minh, P., Lei, W.X., Nong, A.T.Q., Kawaguchi, K., Cuong, T.C., 2022. Zircon U-Pb geochronology and Sr–Nd–Hf isotopic compositions of the felsic dykes from the Dalat zone, southern Vietnam: petrogenesis and geological significance. Int. Geol. Rev. 64 (19), 2822–2836.

Hinz, K., Block, M., Kudrass, H.R., Meyer, H., 1994. Structural elements of the Sulu Sea, Philippines. AAPG Bull. 78, 1146.

Ho, C.S., 1986. A synthesis of the geologic evolution of Taiwan. Tectonophysics 125 (1–3), 1–16.

Hoernle, K., Gill, J., Timm, C., Hauff, F., Werner, R., Garbe-Schönberg, D., Gutjahr, M., 2021. Hikurangi Plateau subduction a trigger for Vitiaz arc splitting and Havre Trough opening (southwestern Pacific). Geology 49 (5), 536–540.

Holloway, N.H., 1982. North Palawan block, Philippines—its relation to Asian mainland and role in evolution of South China Sea. AAPG Bull. 66 (9), 1355–1383.

Hutchison, C.S., 1996. The 'Rajang accretionary prism' and 'Lupar Line' problem of Borneo. Geol. Soc. London Spec. Pub. 106 (1), 247–261.

Hutchison, C.S., 2005. Geology of North-West Borneo: Sarawak. Elsevier, Brunei and Sabah.

Hutchison, C.S., Bergman, S.C., Swauger, D.A., Graves, J.E., 2000. A Miocene collisional belt in north Borneo: uplift mechanism and isostatic adjustment quantified by thermochronology. J. Geol. Soc. 157, 783–793.

Isozaki, Y., Maruyama, S., Furuoka, F., 1990. Accreted oceanic materials in Japan. Tectonophysics 181 (1–4), 179–205.

Isozaki, Y., Aoki, K., Nakama, T., Yanai, S., 2010. New insight into a subduction-related orogen: A reappraisal of the geotectonic framework and evolution of the Japanese Islands. Gondwana Res. 18 (1), 82–105.

Jackson, M.G., Hart, S.R., Konter, J.G., Koppers, A.A., Staudigel, H., Kurz, M.D., Blusztajn, J., Sinton, J.M., 2010. Samoan hot spot track on a "hot spot highway": Implications for mantle plumes and a deep Samoan mantle source. Geochem. Geophys. Geosyst. 11 (12), Q12009.

Jahn, B.M., Chen, P.Y., Yen, T.P., 1976. Rb-Sr ages of granitic rocks in southeastern China and their tectonic significance. Geol. Soc. Am. Bull. 87 (5), 763–776.

Jahn, B.M., Zhou, X.H., Li, J.L., 1990. Formation and tectonic evolution of southeastern China and Taiwan: isotopic and geochemical constraints. Tectonophysics 183 (1–4), 145–160.

Jahn, B.M., Chi, W.R., Yui, T.F., 1992. A late Permian formation of Taiwan (marbles from Chia-Li well no. 1): Pb–Pb isochron and Sr isotopic evidence, and its regional geological significance. J. Geol. Soc. China 35 (2), 193–218.

Jarboe, N., Koppers, A., Tauxe, L., Minnett, R., Constable, C., 2012. The online MagIC Database: data archiving, compilation, and visualization for the geomagnetic, paleomagnetic and rock magnetic communities. AGU Fall. Meeting Abstracts, GP31A-1063.

Jasin, B., 1991. The Sabah Complex-A lithodemic unit (a new name for the Chert-Spilite Formation and its ultramafic association). Warta Geologi 17, 253–259.

Jasin, B., 2018. Radiolarian biostratigraphy of Malaysia. Bull. Geol. Soc. Malaysia 65, 45–58.

Jasin, B., Said, U., 1999. Significance of Early Jurassic Radiolaria from West Sarawak, Malaysia. Proc. Geol. Soc. Malaysia Annual Conference, 491–502.

Jasin, B., Tongkul, F., 2013. Cretaceous radiolarians from Baliojong ophiolite sequence, Sabah, Malaysia. J. Asian Earth Sci. 76, 258–265.

Jasin, B., 2000. Significance of Mesozoic radiolarian chert in Sabah and Sarawak. In Proceedings Geological Society of Malaysia Annual Conference, September 8-9, pp. 123-130.

Ji, W., Lin, W., Faure, M., Chen, Y., Chu, Y., Xue, Z., 2017. Origin of the Late Jurassic to Early Cretaceous peraluminous granitoids in the northeastern Hunan province (middle Yangtze region), South China: Geodynamic implications for the Paleo-Pacific subduction. J. Asian Earth Sci. 141, 174–193.

Jiang, X.Y., Li, X.H., 2014. In situ zircon U-Pb and Hf–O isotopic results for ca. 73 Ma granite in Hainan Island: Implications for the termination of an Andean-type active continental margin in southeast China. J. Asian Earth Sci. 82, 32–46.

Jiang, Y.H., Wang, G.C., Liu, Z., Ni, C.Y., Qing, L., Zhang, Q., 2015. Repeated slab advance–retreat of the Palaeo-Pacific plate underneath SE China. Int. Geol. Rev. 57 (4), 472–491.

Jochum, K.P., Nohl, U., Herwig, K., Lammel, E., Stoll, B., Hofmann, A.W., 2005. GeoReM: a new geochemical database for reference materials and isotopic standards. Geostand. Geoanal. Res. 29 (3), 333–338.

Kakizaki, Y., Weissert, H., Hasegawa, T., Ishikawa, T., Matsuoka, J., Kano, A., 2013. Strontium and carbon isotope stratigraphy of the Late Jurassic shallow marine limestone in western Palaeo-Pacific, northwest Borneo. J. Asian Earth Sci. 73, 57–67.

Karig, D.E., 1983. Accreted terranes in the northern part of the Philippine archipelago. Tectonics 2 (2), 211–236.

Keenan, T.E., 2016. Rapid conversion from spreading to subduction: Structural, geochemical, and geochronological studies in Palawan, Philippines. Ph.D. Thesis. Saint Louis University.

Kirschvink, J., 1980. The least-squares line and plane and the analysis of palaeomagnetic data. Geophys. J. Int. 62 (3), 699–718.

Korenaga, J., 2005. Why did not the Ontong Java Plateau form subaerially?. Earth Planet. Sci. Lett. 234 (3–4), 385–399.

Koymans, M.R., Langereis, C.G., Pastor-Galán, D., van Hinsbergen, D.J., 2016. Paleomagnetism. org: An online multi-platform open source environment for paleomagnetic data analysis. Comput. Geosci. 93, 127-137.

Koymans, M.R., van Hinsbergen, D.J.J., Pastor-Galán, D., Vaes, B., Langereis, C.G., 2020. Towards FAIR paleomagnetic data management through Paleomagnetism. org 2.0. Geochem. Geophys. Geosyst. 21(2), e2019GC008838.

Labis, F.A.C., Payot, B.D., Valera, G.T.V., Pasco, J.A., Dycoco, J.M.A., Tamura, A., Morishita, T., Arai, S., 2021. Melt-rock interaction in the subarc mantle: records from the plagioclase peridotites of the southern Palawan Ophiolite, Philippines. Int. Geol. Rev. 63 (9), 1067–1089.

Lambiase, J.J., Tzong, T.Y., William, A.G., Bidgood, M.D., Brenac, P., Cullen, A.B., 2008. The West Crocker formation of northwest Borneo: A Paleogene accretionary prism. In: Draut, A.E., Clift, P.D., Scholl, D.W. (Eds.), Formation and Applications of the Sedimentary Record in Arc Collision Zones. Geological Society of America, 436. https://doi.org/10.1130/2008.2436(08).

Lapierre, H., Jahn, B.M., Charvet, J., Yu, Y.W., 1997. Mesozoic felsic arc magmatism and continental olivine tholeiites in Zhejiang Province and their relationship with the tectonic activity in southeastern China. Tectonophysics 274 (4), 321–338.

Larsen, H.C., Mohn, G., Nirrengarten, M., Sun, Z., Stock, J., Jian, Z., Zhong, L., 2018. Rapid transition from continental breakup to igneous oceanic crust in the South China Sea. Nat. Geosci. 11 (10), 782–789.

Le Bas, M.L., Le Maitre, R.L., Streckeisen, A., Zanettin, B., IUGS Subcommission on the Systematics of Igneous Rocks, 1986. A chemical classification of volcanic rocks based on the total alkali-silica diagram. J. Petrol. 27 (3), 745–750.

Li, Z.X., Li, X.H., 2007. Formation of the 1300-km-wide intracontinental orogen and postorogenic magmatic province in Mesozoic South China: A flat-slab subduction model. Geology 35 (2), 179–182.

Li, Z.X., Li, X.H., Chung, S.L., Lo, C.H., Xu, X., Li, W.X., 2012b. Magmatic switch-on and switch-off along the South China continental margin since the Permian: Transition from an Andean-type to a Western Pacific-type plate boundary. Tectonophysics 532, 271–290.

Li, X., Li, J., Yu, X., Wang, C., Jourdan, F., 2015. $^{40}Ar/^{39}Ar$ ages of seamount trachytes from the South China Sea and implications for the evolution of the northwestern sub-basin. Geosci. Front. 6 (4), 571–577.

Li, H., Ling, M.X., Li, C.Y., Zhang, H., Ding, X., Yang, X.Y., Fan, W.M., Li, Y.L., Sun, W.D., 2012a. A-type granite belts of two chemical subgroups in central eastern China: Indication of ridge subduction. Lithos 150, 26–36.

Li, Z., Qiu, J.S., Yang, X.M., 2014c. A review of the geochronology and geochemistry of Late Yanshanian (Cretaceous) plutons along the Fujian coastal area of southeastern China: Implications for magma evolution related to slab break-off and rollback in the Cretaceous. Earth-Sci. Rev. 128, 232–248.

Li, C.F., Xu, X., Lin, J., Sun, Z., Zhu, J., Yao, Y., Zhang, G.L., 2014a. Ages and magnetic structures of the South China Sea constrained by deep tow magnetic surveys and IODP Expedition 349. Geochem. Geophys. Geosyst. 15 (12), 4958–4983.

Li, J., Zhang, Y., Dong, S., Johnston, S.T., 2014b. Cretaceous tectonic evolution of South China: A preliminary synthesis. Earth-Sci. Rev. 134, 98–136.

Liu, J.X., Wang, S., Wang, X.L., Du, D.H., Xing, G.F., Fu, J.M., Chen, X., Sun, Z.M., 2020b. Refining the spatio-temporal distributions of Mesozoic granitoids and volcanic rocks in SE China. J. Asian Earth Sci. 201, 104503.

Liu, B., Wu, J.H., Li, H., Wu, Q.H., Evans, N.J., Kong, H., Xi, X.S., 2020a. Geochronology, geochemistry and petrogenesis of the Dengfuxian lamprophyres: Implications for the early Cretaceous tectonic evolution of the South China Block. Geochemistry 80 (2), 125598.

Longerich, H.P., Jackson, S.E., Günther, D., 1996. Inter-laboratory note. Laser ablation inductively coupled plasma mass spectrometric transient signal data acquisition and analyte concentration calculation. J. Anal. Spectrom. 11 (9), 899–904.

Ludwig, K.R., 2003. User's manual for isoplot 3.00, a geochronlogical toolkit for microsoft excel. Berkeley Geochronl. Cent. Spec. Publ. 4, 25–32.

Mahoney, J.J., Storey, M., Duncan, R.A., Spencer, K.J., Pringle, M., 1993. Geochemistry and Age of the Ontong Java Plateau. In: Pringle, M.S., Sager, W.W., Sliter, W.V., Stein, S. (Eds.), The Mesozoic Pacific: Geology, Tectonics, and Volcanism, volume 77. John Wiley & Sons, Inc., American Geophysical Union, Geophysical Monograph Series, pp. 233–261.

McLennan, S.M., Hemming, S., McDaniel, D.K., Hanson, G.N., 1993. Geochemical approaches to sedimentation, provenance, and tectonics. In: Johnsson, M.J., Basu, A. (Eds.), Processes Controlling the Composition of Clastic Sediments, Geological Society of America Special Paper. Geological Society of America, Colorado, pp. 21–40.

Metcalfe, I., 1985. Lower Permian conodonts from the Terbat formation. Sarawak. Warta Geologi. 11, 1–4.

Morley, C.K., 2016. Major unconformities/termination of extension events and associated surfaces in the South China Seas: Review and implications for tectonic development. J. Asian Earth Sci. 120, 62–86.

Moss, S.J., 1998. Embaluh Group turbidites in Kalimantan: evolution of a remnant oceanic basin in Borneo during the Late Cretaceous to Palaeogene. J. Geol. Soc. 155 (3), 509–524.

Mullender, T.A., Frederichs, T., Hilgenfeldt, C., de Groot, L.V., Fabian, K., Dekkers, M.J., 2016. Automated paleomagnetic and rock magnetic data acquisition with an in-line horizontal "2 G" system. Geochem. Geophys. Geosyst. 17 (9), 3546–3559.

Mullender, T.A.T., Van Velzen, A.J., Dekkers, M.J., 1993. Continuous drift correction and separate identification of ferrimagnetic and paramagnetic contributions in thermomagnetic runs. Geophys. J. Int. 114 (3), 663–672.

Muller, C., 1991. Biostratigraphy and geological evolution of the Sulu Sea and surrounding area. In: Silver, E.A., Rangin, C., von Breymann, M.T. (Eds.), Proceedings of the Ocean Drilling Program, Scientific Results, Vol. 124, pp. 121-131.

Nakanishi, M., Tamaki, K., Kobayashi, K., 1992. Magnetic anomaly lineations from Late Jurassic to Early Cretaceous in the west-central Pacific Ocean. Geophys. J. Int. 109 (3), 701–719.

NOAA National Centers for Environmental Information. 2022: ETOPO 2022 15 Arc-Second Global Relief Model. NOAA National Centers for Environmental Information.

Nguyen, T.T.B., Satir, M., Siebel, W., Chen, F., 2004. Granitoids in the Dalat zone, southern Vietnam: age constraints on magmatism and regional geological implications. Int. J. Earth Sci. 93, 329–340.

Niu, Y., Liu, Y., Xue, Q., Shao, F., Chen, S., Duan, M., Guo, P., Gong, H., Hu, Y., Hu, Z., Kong, J., Li, J., Liu, J., Sun, P., Sun, W., Ye, L., Xiao, Y., Zhang, Y., 2015. Exotic origin of the Chinese continental shelf: new insights into the tectonic evolution of the western Pacific and eastern China since the Mesozoic. Sci. Bull. 60 (18), 1598–1616.

Nong, A.T., Hauzenberger, C.A., Gallhofer, D., Dinh, S.Q., 2021. Geochemistry and zircon U-Pb geochronology of Late Mesozoic igneous rocks from SW Vietnam–SE Cambodia: Implications for episodic magmatism in the context of the Paleo-Pacific subduction. Lithos 390, 106101.

Nong, A.T., Hauzenberger, C.A., Gallhofer, D., Skrzypek, E., Dinh, S.Q., 2022. Geochemical and zircon U-Pb geochronological constraints on late Mesozoic Paleo-Pacific subduction-related volcanism in southern Vietnam. Mineral. Petrol. 116 (5), 349–368.

O'Dogherty, L., 1994. Biochronology and palaeontology of Mid-Cretaceous radiolarians from Northern Apennines (Italy) and Betic Cordillera (Spain). Memoires de Geologie (lausanne) 21, 1–413.

Pasco, J.A., Dycoco, J.M.A., Valera, G.T.V., Payot, B.D., Pillejera, J.D.B., Uy, F.A.A.E., Armada, L.T., Dimalanta, C.B., 2019. Petrogenesis of ultramafic-mafic clasts in the Dos Hermanos Mélange, Ilocos Norte: insights to the evolution of western Luzon, Philippines. J. Asian Earth Sci. 184, 104004.

Pearce, J.A., 2008. Geochemical fingerprinting of oceanic basalts with applications to ophiolite classification and the search for Archean oceanic crust. Lithos 100 (1–4), 14–48.

Pessagno, E.A., Newport, R.L., 1972. A technique for extracting Radiolaria from Radiolarian chert. Micropaleontology 18 (2), 231–234.

Qian, X., Yu, Y., Wang, Y., Gan, C., Zhang, Y., Asis, J.B., 2022. Late Cretaceous nature of SW Borneo and paleo-Pacific subduction: New insights from the granitoids in the Schwaner Mountains. Lithosphere 2022 (1), 8483732.

Queaño, K.L., Marquez, E.J., Dimalanta, C.B., Aitchison, J.C., Ali, J.R., Yumul Jr, G.P., 2017. Mesozoic radiolarian faunas from the northwest Ilocos Region, Luzon, Philippines and their tectonic significance. Island Arc 26 (4), e12195.

Rahim, A.R., Konjing, Z., Asis, J., Jalil, N.A., Muhamad, A.J., Ibrahim, N., Munif Koraini, A., Che Kob, R., Mazlan, H., Tjia, H.D., 2017. Tectonostratigraphic terranes of Kudat Peninsula. Sabah. Bull. Geol. Soc. Malaysia 64, 123–139.

Rinke-Hardekopf, L., Dashtgard, S.E., Huang, C., Gibson, H.D., 2021. Application of grouped detrital zircon analyses to determine provenance and closely approximate true depositional age: Early Cretaceous McMurray-Clearwater succession. Canada. Geosci. Front. 12, 877–892.

Rollinson, H.R., Rollinson, H., Pease, V., 2021. Using Geochemical Data: To Understand Geological Processes. Cambridge University Press.

Roser, B., Korsch, R., 1988. Provenance signatures of sandstone-mudstone suites determined using discriminant function analysis of major-element data. Chem. Geol. 67, 119–139.

Rudnick, R.L., Gao, S., 2014. 4.1 - Composition of the Continental Trust. In: Holland, H.D., Turekian, K.K. (Eds.), Treatise in Geochemistry, Second Edition. The Crust. Elsevier, Oxford, pp. 1–51.

Sanfilippo, A., Riedel, W.R., 1985. Cretaceous Radiolaria. In: Bolli, H.M., Saunders, J. B., Perch-Nielsen, K. (Eds.), Plankton Stratigraphy. Cambridge University Press, New York, pp. 631–712.

Schlüter, H.U., Hinz, K., Block, M., 1996. Tectono-stratigraphic terranes and detachment faulting of the South China Sea and Sulu Sea. Mar. Geol. 130 (1–2), 39–78.

Schmidtke, E.A., Fuller, M.D., Haston, R.B., 1990. Paleomagnetic data from Sarawak, Malaysian Borneo, and the late Mesozoic and Cenozoic tectonics of Sundaland. Tectonics 9 (1), 123–140.

Seton, M., Müller, R.D., Zahirovic, S., Gaina, C., Torsvik, T., Shephard, G., Talsma, A., Gurnis, M., Turner, M., Maus, S., Chandler, M., 2012. Global continental and ocean basin reconstructions since 200 Ma. Earth-Sci. Rev. 113 (3–4), 212–270.

Shao, L., Cao, L., Qiao, P., Zhang, X., Li, Q., van Hinsbergen, D.J., 2017. Cretaceous-Eocene provenance connections between the Palawan Continental Terrane and the northern South China Sea margin. Earth Planet. Sci. Lett. 477, 97–107.

Shellnutt, J.G., Lan, C.Y., Van Long, T., Usuki, T., Yang, H.J., Mertzman, S.A., Iizuka, Y., Chung, S.L., Wang, K.L., Hsu, W.Y., 2013. Formation of Cretaceous Cordilleran and post-orogenic granites and their microgranular enclaves from the Dalat zone, southern Vietnam: Tectonic implications for the evolution of Southeast Asia. Lithos 182, 229–241.

Shellnutt, J.G., Ma, G.S.K., Chan, J.S.L., Wong, J.P.M., Wang, K.L., 2023. Early Cretaceous volcanic-arc magmatism in the Dalat-Kratie Fold Belt of eastern Cambodia: implications for the lithotectonic evolution of the Indochina terrane. Front. Earth Sci. 11, 1110568.

Steuer, S., Franke, D., Meresse, F., Savva, D., Pubellier, M., Auxietre, J.L., Aurelio, M., 2013. Time constraints on the evolution of southern Palawan Island, Philippines from onshore and offshore correlation of Miocene limestones. J. Asian Earth Sci. 76, 412–427.

Suggate, S.M., Cottam, M.A., Hall, R., Sevastjanova, I., Forster, M.A., White, L.T., Armstrong, R.A., Carter, A., Mojares, E., 2014. South China continental margin signature for sandstones and granites from Palawan, Philippines. Gondwana Res. 26 (2), 699–718.

Sun, P., Guo, P., Niu, Y., 2021. Eastern China continental lithosphere thinning is a consequence of Paleo-Pacific plate subduction: A review and new perspectives. Earth-Sci. Rev. 218, 103680.

Sun, S.-S., McDonough, W.F., 1989. Chemical and isotopic systematics of oceanic basalts: implications for mantle composition and processes. Geol. Soc. London Spec. Pub. 42, 313–345.

Tauxe, L., Butler, R.F., Van der Voo, R., Banerjee, S.K., 2010. Essentials of Paleomagnetism. University of California Press, California.

Tauxe, L., Watson, G.S., 1994. The fold test: an eigen analysis approach. Earth Planet. Sci. Lett. 122 (3–4), 331–341.

Taylor, B., 2006. The single largest oceanic plateau: Ontong Java–Manihiki–Hikurangi. Earth Planet. Sci. Lett. 241 (3–4), 372–380.

Taylor, B., Hayes, D.E., 1983. Origin and history of the South China Sea basin. Washington DC American Geophysical Union Geophysical Monograph Series 27, 23–56.

Thurow, J., 1988. Cretaceous radiolarians of the North Atlantic Ocean: ODP Leg 103 (Site 638, 640 and 641) and DSDP Legs 93 (Site 603) and 47B (Site 398). In: Boillot, G., Winterer, E.L. (Eds.), Proceedings of the Ocean Drilling Program, Scientific Result 103, 379-418. Texas, College Station.

Thuy, N.T.B., Satir, M., Siebel, W., Vennemann, T., Van Long, T., 2004. Geochemical and isotopic constraints on the petrogenesis of granitoids from the Dalat zone, southern Vietnam. J. Asian Earth Sci. 23 (4), 467–482.

Timm, C., Davy, B., Haase, K., Hoernle, K.A., Graham, I.J., De Ronde, C.E., Woodhead, J., Bassett, D., Hauff, F., Mortimer, N., Seebeck, H.C., Wysoczanski, R.J., Tontini, F.C., Gamble, J.A., 2014. Subduction of the oceanic Hikurangi Plateau and its impact on the Kermadec arc. Nat. Commun. 5 (1), 4923.

Torsvik, T.H., Steinberger, B., Shephard, G.E., Doubrovine, P.V., Gaina, C., Domeier, M., Conrad, C.P., Sager, W.W., 2019. Pacific-Panthalassic reconstructions: Overview, errata and the way forward. Geochem. Geophys. Geosyst. 20 (7), 3659–3689.

Vaes, B., Van Hinsbergen, D.J.J., Van de Lagemaat, S.H.A., Van der Wiel, E., Lom, N., Advokaat, E., Boschman, L.M., Gallo, L.C., Greve, A., Guilmette, C., Li, S.H., Lippert, P.C., Montheil, L., Qayyum, A., Langereis, C., 2023. A global apparent polar wander path for the last 320 Ma calculated from site-level paleomagnetic data. Earth-Sci. Rev. 245, 104547.

Van de Lagemaat, S.H.A., Kamp, P.J.J., Boschman, L.M., Van Hinsbergen, D.J.J., 2023. Reconciling the Cretaceous breakup and demise of the Phoenix Plate with East Gondwana orogenesis in New Zealand. Earth-Sci. Rev. 236, 104276.

Van Der Meer, D.G., Spakman, W., Van Hinsbergen, D.J., Amaru, M.L., Torsvik, T.H., 2010. Towards absolute plate motions constrained by lower-mantle slab remnants. Nat. Geosci. 3 (1), 36–40.

Van der Meer, D.G., Torsvik, T.H., Spakman, W., Van Hinsbergen, D.J.J., Amaru, M.L., 2012. Intra-Panthalassa Ocean subduction zones revealed by fossil arcs and mantle structure. Nat. Geosci. 5 (3), 215–219.

Van Hattum, M.W., Hall, R., Pickard, A.L., Nichols, G.J., 2006. Southeast Asian sediments not from Asia: Provenance and geochronology of north Borneo sandstones. Geology 34 (7), 589–592.

Van Hattum, M.W.A., Hall, R., Pickard, A.L., Nichols, G.J., 2013. Provenance and geochronology of Cenozoic sandstones of northern Borneo. J. Asian Earth Sci. 76, 266–282.

Van Hinsbergen, D.J.J., Schouten, T.L., 2021. Deciphering paleogeography from orogenic architecture: constructing orogens in a future supercontinent as thought experiment. Am. J. Sci. 321 (6), 955–1031.

Vermeesch, P., 2021. Maximum depositional age estimation revisited. Geosci. Front. 12 (2), 843–850.

Vishnevskaya, V.S., 1993. Jurassic and Cretaceous radiolarian biostratigraphy in Russia. In: Blueford, J., Murchey, B. (Eds.), Radiolarian of Giant and Subgiant Fields in Asia. Micropaleontology Special Publ. 6, pp. 175-200.

Waight, T., Fyhn, M.B., Thomsen, T.B., Van Tri, T., Nielsen, L.H., Abatzis, I., Frei, D., 2021. Permian to Cretaceous granites and felsic volcanics from SW Vietnam and S Cambodia: Implications for tectonic development of Indochina. J. Asian Earth Sci. 219, 104902.

Wang, K.L., Lo, Y.M., Chung, S.L., Lo, C.H., Hsu, S.K., Yang, H.J., Shinjo, R., 2012. Age and geochemical features of dredged basalts from Offshore SW Taiwan: The coincidence of Intra-Plate magmatism with the spreading South China Sea. Terrestrial Atmos. Oceanic Sci. 23 (6), 657–669.

Wang, Y., Zhang, A., Qian, X., Asis, J.B., Feng, Q., Gan, C., Zhang, Y., Cawood, P.A., Wang, W., Zhang, P., 2021. Cretaceous Kuching accretionary orogenesis in Malaysia Sarawak: Geochronological and geochemical constraints from mafic and sedimentary rocks. Lithos 400, 106425.

Wang, Y., Qian, X., Asis, J.B., Cawood, P.A., Wu, S., Zhang, Y., Wu, S., Zhang, Y., Feng, Q., Lu, X., 2023. "Where, when and why" for the arc-trench gap from Mesozoic Paleo-Pacific subduction zone: Sabah Triassic-Cretaceous igneous records in East Borneo. Gondwana Res. 117, 117–138.

Wolfart, R., Čepek, P., Gramann, F., Kemper, E., Porth, H., 1986. Stratigraphy of Palawan Island, Philippines. Newslett. Stratigr. 16, 19–48.

Wu, J., Suppe, J., 2018. Proto-South China Sea plate tectonics using subducted slab constraints from tomography. J. Earth Sci. 29, 1304–1318.

Wu, Z., Zhu, W., Shao, L., Xu, C., 2016. Sedimentary facies and the rifting process during the late Cretaceous to early Oligocene in the northern continental margin, South China Sea. Interpretation 4 (3), SP33-SP45.

Xia, L., Li, X., 2019. Basalt geochemistry as a diagnostic indicator of tectonic setting. Gondwana Res. 65, 43–67.

Xu, X., Dong, C., Li, W., Zhou, X., 1999. Late Mesozoic intrusive complexes in the coastal area of Fujian, SE China: the significance of the gabbro-diorite–granite association. Lithos 46 (2), 299–315.

Xu, Y., Yang, Y., Yu, H., Gao, W., Gao, X., Liu, B., Tian, C., Yang, J., Zhang, W., 2020. Geochemistry and petrogenesis of volcanic rocks from the continent-ocean transition zone in northern South China Sea and their tectonic implications. J. Ocean Univ. China 19 (5), 1051–1061.

Xu, Y., Yan, Q.S., Shi, X.F., Yang, J.C., Deng, X.Z., Xu, W.K., Jing, C.L., 2022. Discovery of Late Mesozoic volcanic seamounts at the ocean-continent transition zone in the Northeastern margin of South China Sea and its tectonic implication. Gondwana Res. 120, 111–126.

Yan, Q., Metcalfe, I., Shi, X., 2017. U-Pb isotope geochronology and geochemistry of granites from Hainan Island (northern South China Sea margin): Constraints on late Paleozoic-Mesozoic tectonic evolution. Gondwana Res. 49, 333–349.

Ye, Q., Mei, L., Shi, H., Camanni, G., Shu, Y., Wu, J., Yu, L., Deng, P., Li, G., 2018. The Late Cretaceous tectonic evolution of the South China Sea area: An overview, and new perspectives from 3D seismic reflection data. Earth-Sci. Rev. 187, 186–204.

Yui, T.F., Okamoto, K., Usuki, T., Lan, C.Y., Chu, H.T., Liou, J.G., 2009. Late Triassic-Late Cretaceous accretion/subduction in the Taiwan region along the eastern margin of South China–evidence from zircon SHRIMP dating. Int. Geol. Rev. 51 (4), 304–328.

Yui, T.F., Maki, K., Lan, C.Y., Hirata, T., Chu, H.T., Kon, Y., Yokoyama, T.D., Jahn, B.M., Ernst, W.G., 2012. Detrital zircons from the Tananao metamorphic complex of Taiwan: Implications for sediment provenance and Mesozoic tectonics. Tectonophysics 541, 31–42.

Yumul Jr, G.P., Dimalanta, C.B., Gabo-Ratio, J.A.S., Queaño, K.L., Armada, L.T., Padrones, J.T., Faustino-Eslava, D.V., Payot, B.D., Marquez, E.J., 2020. Mesozoic rock suites along western Philippines: Exposed Proto-South China Sea fragments?. J. Asian Earth Sci.: X, 4, 100031.

Zahirovic, S., Seton, M., Müller, R.D., 2014. The Cretaceous and Cenozoic tectonic evolution of Southeast Asia. Solid Earth 5 (1), 227–273.

Zamoras, L.R., Matsuoka, A., 2001. The Malampaya Sound Group in the Calamian Islands, North Palawan Block (Philippines). J. Geol. Soc. Jpn. 107 (5), XI-XII.

Zamoras, L.R., Matsuoka, A., 2004. Accretion and postaccretion tectonics of the Calamian Islands, North Palawan block, Philippines. Island Arc 13 (4), 506–519.

Zamoras, L.R., Montes, M.G.A., Queano, K.L., Marquez, E.J., Dimalanta, C.B., Gabo, J.A.S., Yumul Jr, G.P., 2008. Buruanga peninsula and Antique Range: two contrasting terranes in Northwest Panay, Philippines featuring an arc–continent collision zone. Island Arc 17 (4), 443–457.

Zhang, A., Asis, J.B., Fang, X., Li, H., Omang, S.A., Chen, M., Fang, Q., Li, D., Peng, T., 2022. Late Cretaceous fore–arc spreading in the northern Kuching Zone of West Borneo, SE Asia: Constraints from the Pakong Mafic Complex. J. Asian Earth Sci. 230, 105189.

Zhang, B., Guo, F., Zhang, X., Wu, Y., Wang, G., Zhao, L., 2019. Early Cretaceous subduction of Paleo-Pacific Ocean in the coastal region of SE China: Petrological and geochemical constraints from the mafic intrusions. Lithos 334, 8–24.

Zhang, X., Pease, V., Skogseid, J., Wohlgemuth-Ueberwasser, C., 2015. Reconstruction of tectonic events on the northern Eurasia margin of the Arctic, from U-Pb detrital zircon provenance investigations of late Paleozoic to Mesozoic sandstones in southern Taimyr Peninsula. Geol. Soc. Am. Bull. B31241, 1.

Zhang, G., Zhang, J., Wang, S., Zhao, J., 2020. Geochemical and chronological constraints on the mantle plume origin of the Caroline Plateau. Chem. Geol. 540, 119566.

Zhao, Q., Yan, Y., Zhu, Z., Carter, A., Clift, P.D., Hassan, M.H.A., Yao, D., Aziz, J.H.A., 2021. Provenance study of the Lubok Antu Melange from the Lupar valley, West Sarawak, Borneo: Implications for the closure of eastern Meso-Tethys?. Chem. Geol. 581, 120415.

Zheng, H., Sun, X., Wang, P., Chen, W., Yue, J., 2019. Mesozoic tectonic evolution of the Proto-South China Sea: A perspective from radiolarian paleobiogeography. J. Asian Earth Sci. 179, 37–55.

Zhou, Y., Carter, A., Wu, J., Yao, Y., Zhu, R., Liu, H., Liu, W., Zhao, Q., Zhu, Z., Yan, Y., Liu, Q., 2023. Nature of the Paleo-Pacific subduction along the East Asian continental margin in the Mesozoic: Insights from the sedimentary record of West Sarawak, Borneo. Geophys. Res. Lett. 50 (8), e2022GL102370.

Zhou, X.M., Li, W.X., 2000. Origin of Late Mesozoic igneous rocks in Southeastern China: implications for lithosphere subduction and underplating of mafic magmas. Tectonophysics 326 (3–4), 269–287.

Zhou, X., Sun, T., Shen, W., Shu, L., Niu, Y., 2006b. Petrogenesis of Mesozoic granitoids and volcanic rocks in South China: a response to tectonic evolution. Episodes J. Int. Geosci. 29 (1), 26–33.

Zhou, D., Wang, W., Wang, J., Pang, X., Cai, D., Sun, Z., 2006a. Mesozoic subduction-accretion zone in northeastern South China Sea inferred from geophysical interpretations. Sci. China Earth Sci. 49 (5), 471.

Zhu, J., Li, S., Jia, Y., Zhang, S., Chen, X., Chen, R., Suo, Y., Cao, X., Jia, Z., Ou, X., Liu, J., Wang, P., Zhou, J., 2022. Links of high velocity anomalies in the mantle to the Proto-South China Sea slabs: Tomography-based review and perspective. Earth-Sci. Rev. 231, 104074.

Zhu, W., Xie, X., Wang, Z., Zhang, D., Zhang, C., Cao, L., Shao, L., 2017. New insights on the origin of the basement of the Xisha Uplift, South China Sea. Sci. China Earth Sci. 60, 2214–2222.

Zijderveld, J.D.A., 1967. A.C. demagnetization of rocks: analysis of results. In: Collinson, D.W., Crees, K.M., Runcorn, S.K. (Eds.), Methods in Paleomagnetism. Elsevier, Amsterdam, pp. 254–286.